

# **Population heterogeneity in the epithelial to mesenchymal transition is controlled by NFAT and phosphorylated Sp1**

Russell Gould<sup>‡</sup> and David M. Bassen, Anirikh Chakrabarti, Jeffrey D. Varner and Jonathan Butcher<sup>‡\*</sup>

Robert Frederick Smith School of Chemical and Biomolecular Engineering and <sup>‡</sup>Nancy E. and Peter C. Meinig School of Biomedical Engineering, Cornell University, Ithaca NY 14853

**Running Title:** Modeling of TGF- $\beta$  induced EMT

**Character count:** 56,659

\*Corresponding author:

Jonathan T. Butcher,

Associate Professor, Nancy E. and Peter C. Meinig School of Biomedical Engineering,  
304 Weill Hall, Cornell University, Ithaca NY, 14853

Email: jtb47@cornell.edu

Phone: (607) 255 - 3575

Fax: (607) 255 - 7330

## Abstract

Epithelial to mesenchymal transition (EMT) is an essential differentiation program during tissue morphogenesis and remodeling. EMT is induced by soluble transforming growth factor  $\beta$  (TGF- $\beta$ ) family members, and restricted by vascular endothelial growth factor family members. While many downstream molecular regulators of EMT have been identified, these have been largely evaluated individually without considering potential crosstalk. In this study, we created an ensemble of dynamic mathematical models describing TGF- $\beta$  induced EMT to better understand the operational hierarchy of this complex molecular program. These models incorporate mass action kinetics within an ordinary differential equation (ODE) framework to describe the transcriptional and post-translational regulatory events driving EMT. Model parameters were estimated from multiple data sets using multiobjective optimization, in combination with cross-validation. TGF- $\beta$  exposure drove the model population toward a mesenchymal phenotype, while an epithelial phenotype was enhanced following vascular endothelial growth factor A (VEGF-A) exposure. Simulations predicted that the transcription factors phosphorylated SP1 and NFAT were master regulators promoting or inhibiting EMT, respectively. Surprisingly, simulations also predicted that a cellular population could exhibit phenotypic heterogeneity (characterized by a significant fraction of the population with both high epithelial and mesenchymal marker expression) if treated simultaneously with TGF- $\beta$  and VEGF-A. We tested this prediction experimentally in both MCF10A and DLD1 cells and found that upwards of 45% of the cellular population acquired this hybrid state in the presence of both TGF- $\beta$  and VEGF-A. We experimentally validated the predicted NFAT/Sp1 signaling axis for each phenotype response. Lastly, we found that cells in the hybrid state had significantly different functional behavior when compared to VEGF-A or TGF- $\beta$  treatment alone. Together, these results establish a predictive mechanistic model of EMT susceptibility, and potentially reveal a novel signaling axis which regulates carcinoma progression through an EMT versus tubulogenesis response.

## **Author Summary**

Tissue formation and remodeling requires a complex and dynamic balance of interactions between epithelial cells, which reside on the surface, and mesenchymal cells that reside in the tissue interior. During embryonic development, wound healing, and cancer, epithelial cells transform into a mesenchymal cell to form new types of tissues. It is important to understand this process so that it can be controlled to generate beneficial effects and limit pathological differentiation. Much research over the past 20 years has identified many different molecular species that are relevant, but these have mainly been studied one at a time. In this study, we developed and implemented a novel computational strategy to interrogate all of the known players in this transformation process to identify which are the major bottlenecks. We determined that NFATc1 and pSP1 are essential for promoting epithelial or mesenchymal differentiation, respectively. We then predicted the existence of a partially transformed cell that exhibits both epithelial and mesenchymal characteristics. We found this partial cell type develops a network of invasive but stunted vascular structures that may be a unique cell target for understanding cancer progression and angiogenesis.

## **1 Introduction**

- 2 The epithelial to mesenchymal transition (EMT) is a broadly participating, evolutionarily  
3 conserved differentiation program essential for tissue morphogenesis, remodeling and  
4 pathological processes such as cancer (Thiery, 2003). During EMT polarized, tightly ad-  
5 hered epithelial cell monolayers are transformed into non-interacting motile mesenchymal  
6 cells that simultaneously degrade and synthesize extracellular matrix (ECM) components  
7 and invade into the underlying tissue space (Stahl & Felsen, 2001). EMT is the funda-  
8 mental initiator of developmental processes such as embryonic gastrulation and valvulo-  
9 genesis (Eisenberg & Markwald, 1995) (also Kalluri J Clin Invest 2009, Thiery Cell 2009).  
10 Transforming growth factor  $\beta$  (TGF- $\beta$ ) family members are important inducers of both de-

11 developmental and pathological EMT (Xu *et al.*, 2009, Zavadil & Böttinger, 2005). Decades  
12 of research has focused on identifying molecular regulators of EMT, but almost all on a  
13 single gene and in a nearly binary yes/no level of qualitative understanding. Medici and  
14 coworkers recently identified a core signaling program by which TGF- $\beta$  isoforms induce  
15 EMT across a variety of cell lines (Medici *et al.*, 2006, 2008). This program involves  
16 carefully orchestrated rounds of gene expression driven by the Smad and Snail families  
17 of transcription factors as well as other key factors such as lymphoid enhancer-binding  
18 factor 1 (LEF-1), nuclear factor of activated T-cells, cytoplasmic 1 (NFATc1), and speci-  
19 fity protein 1 (Sp1). Coregulators such as  $\beta$ -catenin, NF- $\kappa$ B, and the ErbB family of  
20 receptor tyrosine kinases however also participate in EMT regulation, but the degree of  
21 each's influence is difficult to ascertain in isolation (Hardy *et al.*, 2010, Huber *et al.*, 2004,  
22 Jiang *et al.*, 2007, Kim *et al.*, 2002). EMT also exhibits complex temporal dynamics that  
23 are often intractable in gain/loss of function studies. Elucidating the master regulatory ar-  
24 chitecture controlling EMT therefore requires inclusion of these complex overlapping and  
25 non-binary behaviors.

26 Systems biology and mathematical modeling are essential tools for understanding  
27 complex developmental programs like EMT (Ahmed & Nawshad, 2007). Previous com-  
28 putational models of TGF- $\beta$  induced differentiation focused on single biological factors or  
29 EMT in single cells. For example, Chung *et al.*, constructed a model of TGF- $\beta$  receptor  
30 activation and Smad signaling using ordinary differential equations and mass-action ki-  
31 netics. Their model suggested that a reduction of functional TGF- $\beta$  receptors in cancer  
32 cells may lead to an attenuated Smad2 signal (Chung *et al.*, 2009). Similarly, Vilar *et al.*  
33 suggested that specific changes in receptor trafficking patterns could lead to phenotypes  
34 that favor tumorigenesis (Vilar *et al.*, 2006). Although these models provided insight into  
35 the role of receptor dynamics, EMT induction involves many other components, includ-  
36 ing competing second messengers and interconnected transcriptional regulatory loops.  
37 Integrating these additional scales of molecular signaling while maintaining the capacity

38 for robust prediction requires a new and expanded computational and experimental strat-  
39 egy. Data-driven systems approaches (Cirit & Haugh, 2012) or logical model formulations  
40 (Morris *et al.*, 2011) are emerging paradigms that constrain model complexity through  
41 the incorporation of training and validation data. These are interesting techniques be-  
42 cause the data informs model structure (which can be expanded as more data becomes  
43 available). Alternatively, Bailey proposed more than a decade ago that a qualitative un-  
44 derstanding of a complex biological system should not require complete definition of its  
45 structural and parametric content (Bailey, 2001). Shortly thereafter, Sethna and cowork-  
46 ers showed that complex model behavior is often controlled by only a few parameter  
47 combinations, a characteristic seemingly universal to multi-parameter models referred  
48 to as “sloppiness” (Machta *et al.*, 2013). Thus, reasonable model predictions are often  
49 possible with only limited parameter information. Taking advantage of this property, we  
50 developed sloppy techniques for parameter identification using ensembles of determin-  
51 istic models (Song *et al.*, 2010). Furthermore, we proposed that the sloppy behavior of  
52 biological networks may also be seen as a source of cell-to-cell (Lequieu *et al.*, 2011) or  
53 even patient-to-patient heterogeneity (Luan *et al.*, 2010). Recently, Bayesian parameter  
54 identification techniques have also been used to explore cell-to-cell heterogeneity (Hase-  
55 nauer *et al.*, 2011, Kalita *et al.*, 2011), where a population of cells could be viewed as a  
56 dynamic ensemble of context-specific biochemical networks (Creixell *et al.*, 2012).

57 In this study, we developed a family of mechanistic models describing the induction  
58 of EMT by TGF- $\beta$  isoforms in the presence and absence of vascular endothelial growth  
59 factor A (VEGF-A). We incorporated mass action kinetics within an ordinary differential  
60 equation (ODE) framework to describe the EMT interaction network containing 97 gene,  
61 protein or mRNA components interconnected through 169 interactions. A family of model  
62 parameters was estimated using 41 molecular data sets generated in DLD1 colon carci-  
63 noma, MDCKII and A375 melanoma cells using the Pareto optimal ensemble technique  
64 (JuPOETs) multiobjective optimization algorithm. JuPOETs generated an ensemble of

65 approximately 1400 models for analysis. Analysis of the model population suggested that  
66 both MCF10A and DLD1 cells could exhibit phenotypic heterogeneity if treated simultane-  
67 ously with TGF- $\beta$ 1/2 and VEGF-A. This heterogeneity was characterized by a significant  
68 fraction of the population being in a “hybrid state” having both high E-cadherin and high  
69 Vimentin expression. We tested these predictions using qRT-PCR and flow-cytometry  
70 studies in a variety of experimental conditions. Validation studies confirmed that upwards  
71 of 45% of the cellular population could be put into the hybrid state in the presence of both  
72 TGF- $\beta$ 1/2 and VEGF-A. Moreover, this response depended upon both activation of Sp1  
73 by MAPK and NFATc1 transcriptional activity consistent with the predicted molecular sig-  
74 naling. Lastly, the hybrid populations of both DLD1 and MCF10A cells exhibited different  
75 functional behavior than those from either TGF- $\beta$  or VEGF-A treatment. The extent of  
76 ductal branch formation significantly increased with MCF10A cells in the hybrid pheno-  
77 type, compared with cells treated with VEGF-A alone. Together, these results establish  
78 a predictive mechanistic model of EMT susceptibility, and reveal a novel signaling axis,  
79 which possibly regulates carcinoma progression through an EMT versus tubulogenesis  
80 response.

81 **Results**

82 **The model population captured key features of TGF- $\beta$  induced EMT** The EMT model  
83 architecture, based upon curated molecular connectivity, described the expression of 23  
84 genes following exposure to TGF- $\beta$  isoforms and VEGF-A (Fig. 1). The EMT model con-  
85 tained 74 molecular species interconnected by 169 interactions. Model equations were  
86 formulated using either saturation or mass-action kinetics within an ordinary differential  
87 equation (ODE) framework. ODEs and mass action kinetics are common tools to model  
88 biochemical pathways (Chen *et al.*, 2009, Schoeberl *et al.*, 2002, Tasseff *et al.*, 2011).  
89 However, while ODE models can simulate complex intracellular behavior, they require es-  
90 timates for model parameters which are often difficult to obtain. The EMT model had 251  
91 unknown model parameters, 169 kinetic constants and 45 non-zero initial conditions. As  
92 expected, these parameters were not uniquely identifiable given the training data (Gad-  
93 kar *et al.*, 2005). Thus, instead of identifying a single best fit (but uncertain) model, we  
94 estimated a sloppy population of models (each consistent with the training data) by simul-  
95 taneously minimizing the difference between model simulations and 41 molecular data  
96 sets using the Pareto Optimal Ensemble Technique (JuPOETs). The training data were  
97 generated in DLD1 colon carcinoma, MDCKII, and A375 melanoma cells following ex-  
98 posure to TGF- $\beta$  isoforms (Medici *et al.*, 2008). We organized these data sets into 11  
99 objective functions which were simultaneously minimized by JuPOETs. Additionally, we  
100 used 12 molecular data sets generated in HK-2 cells following VEGF-A exposure to train  
101 VEGF-A responsive model processes (Lian *et al.*, 2011). To guard against overfitting,  
102 we augmented the multiobjective optimization with leave-one-out cross validation to in-  
103 dependently estimate both the training and prediction error for each objective. Thus, we  
104 generated 11 different model ensembles. Lastly, we compared model predictions with in-  
105 dependent data sets not used during training (both at the molecular and model population  
106 levels) to evaluate the predictive power of the parameter ensemble.

107 JuPOETs generated a population of probable signaling models which captured the

multiple phases of EMT induction (Fig. 2). JuPOETs sampled well over  $10^4$  probable models during each stage of the cross-validation using global random sampling. From this analysis,  $N \simeq 1400$  models were selected for further analysis. The selected models all had the same possible molecular connectivity, but different values for model parameters. Transcription and translation rates, as well as mRNA and protein degradation terms, were set using physical values from the literature (Milo *et al.*, 2010), and allowed to vary by a scaling factor, see methods. Model selection was based upon Pareto rank, the prediction and training error across all objectives. The model population recapitulated key signaling events following TGF- $\beta$  exposure. We subdivided the response to TGF- $\beta$  exposure into two phases. First, TGF- $\beta$ 1/2 signaling initiated a program which downregulated E-cadherin expression in a MAPK dependent manner while simultaneously upregulating TGF- $\beta$ 3 expression. Second, TGF- $\beta$ 3 secretion initiated an autocrine feedback which upregulated the expression of mesenchymal markers such as Vimentin and key upstream transcription factors such as LEF-1 in a SMAD dependent manner. TGF- $\beta$ 3 expression was also able to sustain  $\beta$ -catenin release by inhibiting its sequestration by the APC complex through PI3K mediated GSK3, which was captured by the model (Fig. 4B). Each phase involved the hierachal expression and/or post-translational modification of several key transcription factors. During the first phase, stimulation with TGF- $\beta$ 1/2 (10 a.u.) activated both the SMAD and MAPK pathways. MAPK activation resulted in the phosphorylation of the transcription factor activator protein 1 (AP-1), which in-turn upregulated the expression of Snail, a well established transcriptional repressor (Fig. 2A). Snail expression was MAPK-dependent; the MEK inhibitor U0126 blocked AP-1 activation and Snail expression following TGF- $\beta$ 1/2 exposure (Fig. 2A, Lane 3). Similar results were obtained for Slug expression, confirming initial activation through the MAPK pathway (data not shown). Overexpression of either Snail or Slug upregulated TGF- $\beta$ 3 expression (Fig. 2C) while simultaneously downregulating E-cadherin expression (Fig. 2F). During the second phase, TGF- $\beta$ 3 secretion and the subsequent autocrine signaling resulted in the

135 upregulation of mesenchymal marker expression. The TGF- $\beta$ 3 induced gene expres-  
136 sion program involves a complex hierarchy of transcriptional and post-translational reg-  
137 ulatory events. Absence of E-cadherin indirectly promoted TGF- $\beta$ 3 expression through  
138 the  $\beta$ -catenin/TCF4 complex following Snail or Slug expression (Fig. 2C, Lane 2 or 3).  
139 Conversely, over-expression of E-cadherin inhibited the TGF- $\beta$ 3 autocrine production by  
140 sequestering cytosolic  $\beta$ -catenin, thereby blocking EMT (Fig. 2C, Lane 4 or 5). TGF- $\beta$ 3  
141 signaled through the Smad pathway to regulate LEF-1 expression and downstream tar-  
142 get EMT genes (Fig. 2G). TGF- $\beta$ 3 (10 a.u.) in combination with downstream inhibitors  
143 (DN-Smad4 and DN-LEF-1) completely inhibited Vimentin expression, while elevating E-  
144 cadherin expression (Fig. 2H,I).

145 The predictive power of the ensemble was tested using both cross validation and by  
146 comparing simulations with data sets not used for model training. In whole, all of our  
147 training objectives were statistically significant (at a 95% confidence interval) compared  
148 to a randomized parameter family ( $N = 100$ ) generated from a random starting point. Con-  
149 versely, we *predicted* all of the training objectives, at a 95% confidence interval compared  
150 to randomized parameters (Wicoxon non-parametric test). The model also captured the  
151 temporal gene expression responses of E-cadherin, pSmad2, and LEF-1 (not used for  
152 model training) to within one-standard deviation (up to the 48 hr time-point) (Fig. 2J-L).  
153 Taken together, the model captured the key signaling events revealed by Medici *et al.*  
154 (Medici *et al.*, 2008) that drive the phenotypic conversion. A listing of objective function  
155 values resulting from training, cross validation and the random parameter control is given  
156 in the supplement (Fig. S1).

157 **Identification of a novel LEF-1 regulator** During model identification, we found that  
158 consistent TGF- $\beta$  induced EMT from a stable epithelial cell population required an addi-  
159 tional regulatory protein. This protein, which we called hypothetical regulator 1 (YREG1),  
160 was required to mediate between SNAIL/SLUG transcriptional activity and the upregu-  
161 lation of LEF-1 expression following TGF- $\beta$ 1/2 exposure. SNAIL/SLUG are well known

transcriptional repressors (Dhasarathy *et al.*, 2011, Hemavathy *et al.*, 2000a,b), although there are a few studies which suggest that at least SNAIL can also act as a transcriptional activator (Guaita *et al.*, 2002). In the model, we assumed the expression of SNAIL/SLUG was likely regulated by AP1/SP1 (Jackstadt *et al.*, 2013). Thus, upon receiving direct SNAIL/SLUG and TGF- $\beta$ 3 signals, the model predicted enhanced SNAIL/SLUG expression, consistent with experimental observations. TGF- $\beta$ 1/2 stimulation also induces LEF-1 expression. However, literature evidence suggested that LEF-1 expression was not strongly dependent upon AP1/SP1 activity (Eastman & Grosschedl, 1999). Thus, either SNAIL/SLUG are acting as inducers (contrary to substantial biochemical evidence) or, they are repressing the expression of an intermediate repressor. Given the biochemical evidence supporting SNAIL/SLUG as repressors, we created the hypothetical YREG1 repressor whose expression is downregulated by SNAIL/SLUG. The literature data therefore suggested that YREG1 had two transcriptional targets, LEF-1 and TGF- $\beta$ 3. By adding this regulator, our simulations became consistent with training and literature data. Medici *et al.* suggested that feedback between  $\beta$ -catenin and LEF-1 was likely, although this feedback had yet to be identified (Medici *et al.*, 2008). Low levels of YREG1 expression were present in all simulations to regulate the formation of the  $\beta$ -catenin-LEF-1 complex. To test the effect of YREG1 on the epithelial population, we conducted over-expression and knockdown simulations on untreated cells (Fig. 4C and 4D). In the absence of YREG1, the population of models failed to consistently retain a stable epithelial state (Fig. 4D). Conversely, YREG1 amplification revealed an enhanced epithelial phenotype, while some inherently transformed cells moved towards a hybrid phenotype (Fig. 4C). Elevated YREG1 repressed LEF-1 and TGF- $\beta$ 3 expression, thereby not allowing free  $\beta$ -catenin to form the  $\beta$ -catenin-LEF-1 complex, or TGF- $\beta$ 3 induced SMAD activation. Taken together, low YREG1 expression was required for the maintenance of a stable epithelial phenotype that was simultaneously inducible across TGF- $\beta$ 1/2, TGF- $\beta$ 3 and SNAIL/SLUG transfection, as seen in the training objectives.

189 **TGF- $\beta$ 1/2 and VEGF-A exposure promotes phenotype heterogeneity through NFATc  
190 and phosphorylated Sp1** While we captured the central tendency of many of the molec-  
191 ular features of EMT induction following TGF- $\beta$ 1/2 exposure, an often neglected but im-  
192 portant emergent feature of developmental and pathological programs is population het-  
193 erogeneity (Park *et al.*, 2010). We (and others) have previously hypothesized that deter-  
194 ministic model ensembles can simulate population behavior, at least at a course grained  
195 level (Lequieu *et al.*, 2011). We tested this hypothesis by analyzing the response of the  
196 population of EMT models to extracellular cues and then comparing this response to flow  
197 cytometry studies. We quantified the phenotypic response of the individual members of  
198 the ensemble to TGF- $\beta$ 1/2 stimulation for two downstream phenotypic markers, Vimentin  
199 (mesenchymal) and E-cadherin (epithelial) following the addition of TGF- $\beta$ 1/2 alone (Fig.  
200 3), and/or VEGF-A in combination with NFATc inhibitors (Fig. 3).

201 We identified model subpopulations that exhibited different behaviors following expo-  
202 sure to TGF- $\beta$ 1/2 (Fig. 3B). Analysis of the molecular signatures of these subpopulations  
203 suggested the abundance, localization and state of the Sp1, AP-1 and NFATc transcription  
204 factors controlled population heterogeneity. The majority of models (>80%) responded  
205 to treatment, moving away from the untreated population (Fig 3A-F, gray). These mod-  
206 els showed the classically expected behavior, a switch from an epithelial to mesenchy-  
207 mal phenotype following TGF- $\beta$ 1/2 exposure. Some models resembled untreated cells;  
208 they had elevated phosphorylated Sp1, relative to non-induced cells, which decreased E-  
209 cadherin expression through Slug-mediated inhibition, which in turn increased Vimentin  
210 expression through TGF- $\beta$ 3 autocrine signaling and the liberation of  $\beta$ -catenin. How-  
211 ever, the most biologically interesting behavior was exhibited by cells achieving a hybrid  
212 phenotype, most notable in a dual treatment condition (3C, black arrow), but also present  
213 in a small percentage of untreated cells (Fig. 3B, gray arrow). Models with this hybrid  
214 phenotype had elevated Sp1 and NFAT transcriptional activity, resulting in simultaneously  
215 increased Vimentin and E-cadherin expression (Fig. 4A).

216 To better understand the hybrid phenotype, we simulated the response of the model  
217 population to TGF- $\beta$ 1/2 and VEGF-A treatment with and without NFATc inhibitors (Fig.  
218 3). As expected, stimulation with VEGF-A (50 a.u.) maintained an epithelial population  
219 (Fig. 3A), while TGF- $\beta$ 1/2 (10 a.u.) exposure shifted the population from an epithelial  
220 to a mesenchymal phenotype (Fig. 3B). On the other hand, combined stimulation with  
221 TGF- $\beta$ 1/2 (10 a.u.) and VEGF-A (50 a.u.) increased both E-cadherin and Vimentin ex-  
222 pression, resulting in a hybrid phenotype with both epithelial and mesenchymal character-  
223 istics (Fig. 3C). Vimentin expression was correlated with high levels of nuclear phospho-  
224 rylated Sp1, following TGF- $\beta$ 1/2 exposure. Conversely, elevated E-cadherin expression  
225 depended upon the activity of NFAT transcription factors downstream of VEGF-A stimula-  
226 tion. To further isolate the role of NFAT on this hybrid state, we simulated the inhibition of  
227 NFAT transcriptional activity across all conditions (all else being equal). NFAT inhibition  
228 in combination with VEGF-A or TGF- $\beta$ 1/2 treatments blocked increased E-cadherin ex-  
229 pression in the case of VEGF-A (Fig. 3D), but did not influence TGF- $\beta$ 1/2 signaling (Fig.  
230 3E). Lastly, NFATc inhibition in combination with simultaneous TGF- $\beta$ 1/2 and VEGF-A  
231 exposure repressed nearly all E-cadherin expression, shifting nearly the entire population  
232 towards a mesenchymal phenotype (Fig. 3F). Taken together, high levels of nuclear local-  
233 ized phosphorylated Sp1 correlated with Vimentin expression, while NFATc transcriptional  
234 activity was critical for maintaining E-cadherin expression in the presence of competing  
235 signals.

236 **Combined TGF- $\beta$ 2 and VEGF-A exposure drives heterogeneity in MCF10A and**  
237 **DLD1 cells** The EMT model simulations suggested the transcriptional activity of NFATc  
238 and Sp1 could be independently tuned to generate a hybrid cell population with both  
239 epithelial and mesenchymal characteristics. To test this hypothesis, we exposed either  
240 quiescent epithelial (MCFA10, Fig. 5) or transformed epithelial cells (DLD1, Fig. S2) to  
241 combinations of TGF- $\beta$ 1/2 and/or VEGF-A. As expected, TGF- $\beta$ 1/2 treatment (10ng/ml)  
242 increased Slug and Vimentin expression, while repressing E-cadherin expression both at

the transcript and protein levels in MCF10A (Fig. 5A-B) and DLD1 cells (Fig. S3C). Both MCF10A (Fig. 5C) and DLD1 cells (Fig. S2E,G) transitioned from quiescent cobble-stone morphology to spread spindle shapes, consistent with EMT. As predicted, we found increased nuclear localization of phosphorylated Sp1 following TGF- $\beta$ 1/2 stimulation in both MCF10A (Fig. 5B,C) and DLD1 cells (Fig. S2E,F). Consistent with model predictions, VEGF-A (50ng/ml) treatment increased the abundance of NFATc1 and E-cadherin at both the transcript and protein level in both MCF10A (Fig. 5A) and DLD1 cells (Fig. S2). We also found that NFATc1 nuclear localization significantly increased in both MCF10 (Fig. 5B,C) and DLD1 (Fig. S2C,E) cells treated with VEGF-A. Interestingly, combining VEGF-A (50ng/ml) with TGF- $\beta$ 1/2 (10ng/ml) resulted in significantly elevated expression of both E-cadherin and Vimentin at the transcript and protein levels in both MCF10A (Fig. 5A,B) and DLD1 cells (Fig. S2-S3). NFATc1 expression increased, while Sp1 expression was similar to the TGF- $\beta$ 1/2 case alone (Fig. 5A-B and Fig. S2D,E), supporting their independent regulation. The expression of Slug, and Vimentin significantly increased, while E-cadherin levels were increased in MCF10A cells (Fig. 5A) and maintained at control levels in DLD1 cells (Fig. S2D). As predicted, nuclear co-localization of both NFATc1 and phosphorylated Sp1 were apparent in MCF10A (Fig. 5B,C) and DLD1 (Fig. S2E,F) cells treated with both ligands. Taken together, combined VEGF-A and TGF- $\beta$ 1/2 treatment elicited a hybrid phenotype expressing both mesenchymal and epithelial characteristics in both MCF10A and DLD1 cells. This phenotype was driven by the transcriptional activity of two key transcription factors, Sp1 and NFATc, which could be modulated independently by TGF- $\beta$ 1/2 and VEGF-A exposure.

Our phenotypic analysis predicted that NFATc transcriptional activity was critical to maintaining E-cadherin expression in the presence of both VEGF-A and TGF- $\beta$ 1/2. We experimentally tested this hypothesis by exposing both MCF10A (Fig. 5E,F) and DLD1 cells (Fig. S3) to combinations of VEGF-A and TGF- $\beta$ 1/2 in the presence or absence of VIVIT, a soluble peptide inhibitor of NFATc transcriptional activity (Aramburu *et al.*,

270 1999). Treatment with VEGF-A (50ng/ml) and VIVIT (10 $\mu$ M) in MCF10A cells significantly  
271 reduced E-cadherin expression compared to VEGF-A alone (Fig. 5D,E). Co-treatment  
272 with VIVIT and TGF- $\beta$ 1/2 did not enhance EMT capacity of MCF10A cells above that  
273 of TGF- $\beta$ 1/2 alone (Fig. 5A,B,E). Likewise, VIVIT in combination with both TGF- $\beta$ 1/2  
274 and VEGF-A resulted in a loss of E-cadherin gene and protein expression, while Slug  
275 and Vimentin levels remained increased (Fig. 5D,E). Quantitative flow cytometry con-  
276 firmed these results in both MCF10A (Fig. 5F) and DLD1 cells (Fig. S3C). Both epithelial  
277 cell lines initially had high levels of E-cadherin expression, and low Vimentin abundance  
278 (Q1-99.5%), but both MCF10A and DLD1 cells shifted from an epithelial to mesenchymal  
279 phenotype (Q1-33.4%, Q4-42.8%) following TGF- $\beta$ 1/2 exposure. As expected, NFATc  
280 nuclear localization was repressed with VIVIT treatment regardless of ligand stimulation,  
281 while the abundance of nuclear phosphorylated Sp1 increased for both TGF- $\beta$ 1/2 and  
282 TGF- $\beta$ 1/2 + VIVIT conditions (Fig. 5C,E). Combined TGF- $\beta$ 1/2 and VEGF-A increased  
283 both Vimentin and E-cadherin expression (Q1-42.1%, Q2-52.3%) compared to TGF- $\beta$ 1/2  
284 alone. Together, these results demonstrate that NFATc and phosphorylated Sp1 are criti-  
285 cal for regulating E-cadherin and Vimentin expression during phenotype heterogeneity in  
286 MCF10A and DLD1.

287 **Ductal branching during acini formation is dependent upon phenotype heterogene-  
288 ity in MCF10A and DLD1 cells** We finally employed established three-dimensional  
289 (3D) *in vitro* models of invasion, migration, compaction, and tubulogenesis (Dhimolea  
290 *et al.*, 2010) to determine the functional consequences of the hybrid phenotype (Fig. 6).  
291 MCF10A and DLD1 cells were aggregated via hanging drop, placed on the surface of a  
292 collagen gel, and cultured for 72 hrs under various biochemical treatments. TGF- $\beta$ 1/2  
293 stimulation significantly enhanced cell matrix invasion and matrix compaction, while in  
294 contrast VEGF-A stimulation promoted surface migration but no invasion or compaction  
295 (Fig. 6B-D). Interestingly, combined TGF- $\beta$ 1/2 and VEGF-A stimulation significantly in-  
296 creased cell migration potential above that of VEGF-A alone while maintaining 3D matrix

compaction, though with decreased magnitude compared to TGF- $\beta$ 1/2 alone. Inhibition of NFATc transcriptional activity by VIVIT decreased migration following treatment with VEGF-A alone (Fig. 6B). Co-treatment of VIVIT significantly decreased migration, while complementarily increasing invasion and compaction, when MCF10A cells were stimulated with both VEGF-A and TGF- $\beta$ 1/2 (Fig. 6B-D). The responses of DLD1 cells followed a similar trend to MCF10A, although the magnitudes of migration, invasion, and compaction were less. Cell circularity within 3D gels strongly and negatively correlated with both invasion and compaction regardless of treatment (Fig. 6E). Circularity refers to the morphology of the cells. In general, a quiescent epithelial cells assumes a circular morphology in culture, while an active mesenchymal cell is highly elongated. The circularity index, a common means of quantifying cell morphology, relates cell area to perimeter. A perfect circle has a circularity index equal to 1.0, while a straight line has a circularity index equal to 0.0, see Butcher et al. (Butcher *et al.*, 2004). TGF- $\beta$ 1/2 treatment alone resulted in irregular and spindle shaped morphology, while VEGF-A exposure promoted round quiescent cells (Fig. 6A). Combined VEGF-A and TGF- $\beta$ 1/2 promoted morphology between these extremes. VIVIT mediated NFATc inhibition significantly reduced the circularity index, similar to TGF- $\beta$ 1/2 treatment (Fig. 6F). VEGF-A treatment also induced the formation of tubular structures (acini), but the number of tubular branches relative to total acini was significantly increased upon combined TGF- $\beta$ 1/2 and VEGF-A. No tubular structures were identified within the DLD1 constructs during the 7 day tubulogenesis endpoints, supporting that MCF10A and DLD1 cells have some cell-type specific EMT sensitivity despite their underlying competency for acquiring a heterogeneous phenotype. This suggests that initial EMT sensitivity of a cell influences downstream functional response from TGF- $\beta$  and VEGFA stimulation. Together, these results establish that VEGF-A and TGF- $\beta$ 1/2 ligand concentrations potentiate between acini and ductal branch formation in 3D culture, and are dependent upon NFATc activity.

323 **Discussion**

324 In this study, we developed a family of mechanistic models describing the induction of  
325 EMT by TGF- $\beta$  isoforms in the presence and absence of VEGF-A. The signaling architec-  
326 ture encoded in the model, which contained 74 molecular species interconnected by 169  
327 interactions, described the expression of 23 genes in response to growth factor stimula-  
328 tion. This simulation incorporates an unprecedented level of detail compared to previous  
329 models, but as a consequence created a large number of unknown model parameters.  
330 Because these parameters could not be estimated uniquely apriori, we estimated an en-  
331 semble of likely parameters using the JuPOETs multiobjective optimization framework.  
332 The model population was trained and cross-validated to prescribe biological significance  
333 using 41 data sets generated in DLD1 colon carcinoma, MDCKII, and A375 melanoma  
334 cell lines (Medici *et al.*, 2008). Analysis of this population predicted possible phenotypic  
335 modes (and their associated signaling) that cells could exhibit when stimulated with TGF-  
336  $\beta$  and/or VEGF-A. The most novel hypothesis generated from the analysis was that cells  
337 could operate in a hybrid state defined by both epithelial and mesenchymal traits when  
338 stimulated simultaneously with TGF- $\beta$  and VEGF-A. We tested this hypothesis in MCF10A  
339 and DLD1 cells stimulated with combinations of TGF- $\beta$  and VEGF-A. As expected, in  
340 the presence of TGF- $\beta$  or VEGF-A alone, MCF10A and DLD1 cells were either mes-  
341 enchymal or epithelial, respectively. However, with both TGF- $\beta$  and VEGF-A, MCF10A  
342 and DLD1 cells exhibited a hybrid phenotype, having both epithelial and mesenchymal  
343 characteristics. Furthermore, we found that functional traits such as tubulogenesis and  
344 ductal branching were different for cells in this hybrid phenotype. Together, this study  
345 established a predictive model of EMT induction, determined that deterministic model  
346 ensembles could predict population heterogeneity, and proved the existence of a unique  
347 hybrid phenotype resulting from the simultaneous integration of extracellular growth factor  
348 signals.

349 Cells routinely process a multitude of signals simultaneously, especially when coordi-

nating developmental or pathological programs. For example, oncogenic cells integrate both mechanical and chemical cues in their local microenvironment during tumorigenesis, including cytokines VEGF and TGF- $\beta$  (Hong *et al.*, 2013). VEGF-A mediates pathological angiogenic remodeling of tumors (Nagy *et al.*, 2007), while TGF- $\beta$  can elicit both protective and oncogenic responses (Ferrara, 2002, Willis & Borok, 2007). While much research has tested signaling pathways individually, far less is understood about combinatorial stimulation, such as with both VEGF-A and TGF- $\beta$ . Recent *in vitro* and *in vivo* evidence has suggested that epithelial cells can exhibit heterogeneous phenotypes in addition to classically defined epithelial or mesenchymal states (Polyak & Weinberg, 2009, Strauss *et al.*, 2011). For example, expression profiling in human epithelial cancer cell lines demonstrated a spectrum of phenotypes, including some that expressed both E-cadherin and Vimentin simultaneously (Neve *et al.*, 2006, Welch-Reardon *et al.*, 2014). Zajchowski *et al.*, speculated that these expression profiles were somehow important for maintaining epithelial properties, while simultaneously allowing other functional behavior such as proliferation and migration (Zajchowski *et al.*, 2001). Whether and how heterogeneous phenotypes arise and participate in cancer progression, as well as their response to pharmacological inhibition are fundamental questions that should receive increased attention. In this study, we determined that a hybrid phenotype could be obtained through combined treatment with VEGF-A and TGF- $\beta$ , both common factors localized in the tumor microenvironment. Furthermore, our systematic simulation-experimentation strategy identified that the transcriptional activity of Sp1 and NFATc were the critical factors controlling this phenotypic heterogeneity. Several studies have highlighted the importance of NFATc as a key transcription factor involved in cell growth, survival, invasion, angiogenesis and cancer (Mancini & Toker, 2009). For example, proliferation and anchorage-independent growth of pancreatic tumor cells is dependent on calcineurin and NFATc1 activity, consistent with the high levels of nuclear NFATc1 found in pancreatic tumors (Singh *et al.*, 2010). Likewise, our results found that VEGF-A was a potent inducer of

377 NFATc1 expression, which may be required for epithelial cell migration and tubulogenesis.  
378 Although specific NFATc isoforms were not distinguished in the model, our simulations  
379 suggested that NFATc transcriptional activity was capable of maintaining epithelial traits,  
380 even during TGF- $\beta$  induced EMT. Experimentally, we found that E-cadherin expression  
381 was dependent upon NFATc dephosphorylation in response to simultaneous VEGF-A and  
382 TGF- $\beta$ 1/2 treatment. Thus, these results support the hypothesis that NFATc activity plays  
383 a critical role in maintaining cell-cell contacts, even during partial EMT.

384 Epithelial cells reproduce tissue-like organization when grown in a three-dimensional  
385 extracellular matrix (ECM) environment, and therefore are an attractive model to study  
386 morphogenic mechanisms. It is well established that MCF10A cells form structures that  
387 closely resemble acini (multi-lobed cluster of cells) in three-dimensional *in vitro* cultures  
388 (Debnath *et al.*, 2003). It has been postulated that a cellular response reminiscent of  
389 partial EMT underlies this process, stimulating further branching and formation of acini  
390 (Pearson & Hunter, 2007). Normally well controlled process such as tubulogenesis can  
391 be co-opted by cancer cells to break away from a primary lesion and invade through  
392 the surrounding stroma (O'Brien *et al.*, 2004). However, by retaining a transient hybrid  
393 EMT-like state, clusters of these tube-forming tumor cells can reform at a high rate af-  
394 ter invasion, possibly explaining why invasive human carcinomas frequently appear to be  
395 cellular collections with varying degrees of gland-like differentiation (Debnath & Brugge,  
396 2005). In this study, we showed that our predicted hybrid phenotype generated by sim-  
397 taneous treatment of epithelial cells with VEGF-A and TGF- $\beta$  possessed altered migra-  
398 tion and invasion, which enhanced tubular branching. A salient feature of this behavior,  
399 however, was the retention of cell-cell contacts that allowed cells to migrate without com-  
400 pletely dissociating from their neighbors. Thus, our results support a mechanism in which  
401 hybrid cells can maintain some functional characteristics of epithelial cells such as cell-  
402 cell adhesion, which are normally lost in a fully differentiated mesenchymal state. The  
403 tumor microenvironment contains many soluble signals simultaneously, including VEGF

404 and TGF- $\beta$ . Thus, it is likely that some cancerous epithelial cells could exhibit hybrid EMT  
405 phenotypic states. This may explain why fibroblastoid morphology, a classical feature of  
406 EMT, is not commonly observed in human carcinomas (Debnath & Brugge, 2005). This  
407 study focused on the combinatorial effects of two very different ligand families present to-  
408 gether in the tumor environment. Additional modeling studies are required to unravel the  
409 global response of epithelial cells to the full spectrum of chemical, substrate, and mechan-  
410 ical cues. The simulation strategy presented here is readily adaptable to larger species  
411 sets, with the major advantage that experimentally testable hypotheses can be generated  
412 regarding how signals get integrated to produce global cellular response. Furthermore, by  
413 simulating multiple ensembles of parameter sets, subpopulations across a constellation of  
414 phenotypes can be created and mined for common and/or divergent signaling character-  
415 istics. This is a significant advantage over forced convergence to a single unique solution  
416 and thereby generating a potentially non-physiological homogeneous population.

417 The deterministic population of EMT models predicted heterogeneous behavior that  
418 was qualitatively consistent with experimental studies. There is a diversity of algorithmic  
419 approaches to estimate model parameters (Moles *et al.*, 2003), as well as many strategies  
420 to integrate model identification with experimental design (Rodriguez-Fernandez *et al.*,  
421 2013, Villaverde & Banga, 2014). However, despite these advances, the identification of  
422 models describing intracellular network behavior remains challenging. There are differ-  
423 ent schools of thought to deal with this challenge. One school has focused on model  
424 reduction. Data-driven approaches (Cirit & Haugh, 2012), boolean (Choi *et al.*, 2012) or  
425 other logical model formulations (Morris *et al.*, 2011, Terfve *et al.*, 2012) are emerging  
426 paradigms that constrain model complexity by the availability of the training and validation  
427 data. Other techniques such as constraints based modeling, which is commonly used to  
428 model metabolic networks, have also been applied to model transcriptional networks, al-  
429 though primarily in lower eukaryotes and prokaryotes (Hyduke & Palsson, 2010). These  
430 techniques (and many others, see review (Wayman & Varner, 2013)) are certainly ex-

citing, with many interesting properties. Here, we used a traditional approach of mass action kinetics within an ordinary differential equation framework that also included transfer functions to simplify scenarios where reactions involving one species are controlled by several others (e.g. E-cadherin transcription). The identification problem for the EMT model was massively underdetermined. This is not uncommon for differential equation models, especially those that are highly mechanistic. Of course, we could have discarded mechanism or reduced the model scope to decrease the complexity of the identification problem. However, a central criticism leveled by biologists is that model simplification is often done at the cost of biological reality, or done for reasons of computational expediency (Sainani, 2012). To avoid this criticism, we systematically identified an ensemble of likely models each consistent with the training data, instead of a single but uncertain best fit model. Previously, we (and others) have suggested that deterministic ensembles could model heterogeneous populations in situations where stochastic computation was not feasible (Lequieu *et al.*, 2011). Population heterogeneity using deterministic model families has previously been explored for bacterial growth in batch cultures (Lee *et al.*, 2009). In that case, distributions were generated because the model parameters varied over the ensemble, i.e., extrinsic noise led to population heterogeneity. In this study, parameters controlling physical interactions such as disassociation rates or the rate of assembly or degradation of macromolecular machinery such as ribosomes were widely distributed over the ensemble. Population heterogeneity can also arise from intrinsic thermal fluctuations, which are not captured by a deterministic population of models (Swain *et al.*, 2002). Thus, deterministic ensembles, provide a coarse-grained or extrinsic-only ability to simulate population diversity. Despite this limitation, our prediction of phenotypic heterogeneity (and the underlying signaling events responsible for the heterogeneity) was consistent with experimental observations. This suggested that deterministic ensembles could simulate disease or developmental processes in which heterogeneity plays an important role, without having to resort to stochastic simulation.

458 A common criticism of ODE modeling has been the poorly characterized effect of  
459 structural and parametric uncertainty. In this study, parametric uncertainty was addressed  
460 by developing an ensemble of probable models instead of a single best-fit but uncertain  
461 model using multiobjective optimization. While computationally complex, multiobjective  
462 optimization is an important tool to address qualitative conflicts in training data that arise  
463 from experimental error or cell line artifacts (Handl *et al.*, 2007). On the other hand, struc-  
464 tural uncertainty is defined as uncertainty in the biological connectivity. The EMT model  
465 connectivity was assembled from an extensive literature review. However, several poten-  
466 tially important signaling mechanisms were not included. First, we identified a potential  
467 gap in biological knowledge surrounding the regulation of LEF-1 expression, that was filled  
468 by the addition of the hypothetical YREG1 transcriptional repressor. The LEF-1 transcrip-  
469 tion factor is expressed in tissues that undergo EMT during embryogenesis (Nawshad &  
470 Hay, 2003, Vega *et al.*, 2004), and has been suggested to promote an invasive phenotype  
471 in cancer cells (Cano *et al.*, 2000, Kim *et al.*, 2002). Low levels of YREG1 were important  
472 for stabilizing the interaction between LEF-1 and  $\beta$ -catenin, while elevated levels inhibited  
473 EMT by downregulating LEF-1 transcriptional activity. Recent evidence has established a  
474 complex role of Amino terminal Enhancer of Split (AES) and Groucho/TLE on suppress-  
475 ing LEF-1 activity. AES opposes LEF-1 transcriptional activation while Groucho/TLE binds  
476 with LEF-1 for a histone deacetylase repression. In addition,  $\beta$ -catenin directly displaces  
477 Groucho/TLE repressors from TCF/LEF-1 in Wnt-mediated transcription activation (Arce  
478 *et al.*, 2009, Grumolato *et al.*, 2013). Our model agrees with this newly discovered feed-  
479 back system, as YREG1 regulates LEF-1 activity leading to EMT stabilization.

480 Recent evidence has also suggested an essential role of NF- $\kappa$ B in epithelial trans-  
481 formation. NF- $\kappa$ B may influence Snail expression through the AKT pathway and directly  
482 stabilize Snail activity (Wu *et al.*, 2009). This is particularly important for integrating in-  
483 flammation pathways, such as interleukin-6 (IL-6) and tumor necrosis factor- $\alpha$  (TNF- $\alpha$ ),  
484 which have been linked to EMT in pathological conditions (Sullivan *et al.*, 2009). Other

485 pathways such as Notch have also been shown to act synergistically with TGF- $\beta$  to ex-  
486 press Slug in the developing embryo (Niessen *et al.*, 2008). Lastly, while we have modeled  
487 classical protein signaling, we have not considered the role of regulatory RNAs on EMT.  
488 There is growing evidence that microRNAs (miRNAs) play a strong role in EMT, where  
489 several miRNAs, for example miR-21 and miR-31 are strongly associated with TGF- $\beta$  ex-  
490 posure (Bullock *et al.*, 2012). Addressing missing structural components like these, could  
491 generate more insight into TGF- $\beta$  signaling and its role in phenotypic transformation.

492 **Materials and Methods**

493 The model code and parameter ensemble is freely available under an MIT software li-  
494 cense and can be downloaded from <http://www.varnerlab.org>.

495 **Signaling network connectivity** The EMT model described the gene expression pro-  
496 gram resulting from TGF- $\beta$  and VEGF-A signaling in a prototypical epithelial cell. The  
497 TGF- $\beta$ -EMT network contained 97 nodes (proteins, mRNA or genes) interconnected by  
498 251 interactions. The network connectivity was curated from more than 40 primary liter-  
499 ature sources in combination with on-line databases (Jensen *et al.*, 2009, Linding *et al.*,  
500 2007). The model interactome was not specific to a single epithelial cell line. Rather, we  
501 assembled canonical pathways involved in TGF- $\beta$  and VEGF-A signaling, defaulting to  
502 human connectivity when possible. Using a canonical architecture allowed us to explore  
503 general features of TGF- $\beta$  induced EMT without cell line specific artifacts. On the other  
504 hand, because of the canonical architecture, we can test the model against several cell  
505 lines to test the generality of our conclusions.

506 Our signaling network reconstruction was based on Medici *et al.* who identified the  
507 pathways through which MDCKII, DLD1 colon carcinoma, and A375 melanoma cells tran-  
508 sition towards a mesenchymal phenotype (Medici *et al.*, 2008). Sequential activation of  
509 MAPK and Smad pathways were initiated upon addition of TGF- $\beta$ 1/2. Briefly, TGF- $\beta$ 2  
510 signals through the RAS-RAF-MEK-ERK pathway to up-regulate Snail and Slug expres-  
511 sion (Medici *et al.*, 2006). Snail, a known repressor of junctional proteins, inhibits the ex-  
512 pression of E-cadherin (Cano *et al.*, 2000). This initial repression of E-cadherin leads to a  
513 release of  $\beta$ -catenin from the cell membrane. This release of  $\beta$ -catenin can then translo-  
514 cate to the nucleus and form transcriptional complexes with TCF-4 to drive TGF- $\beta$ 3 ex-  
515 pression (Medici *et al.*, 2008). The PI3K to GSK3 pathway was included and acted as  
516 an activating mechanism of  $\beta$ -catenin signaling through TGF- $\beta$ 3 signaling (Medici *et al.*,  
517 2008). GSK3 is known to act on  $\beta$ -catenin signaling through the ubiquitin-proteasome  
518 pathway (Larue & Bellacosa, 2005, Zhou *et al.*, 2004). Thereby, further  $\beta$ -catenin release

519 also resulted from by TGF- $\beta$ 3 signals to the cells interior by binding to type II receptors,  
520 which form heterodimers with type I receptors (ALK5) (Derynck & Zhang, 2003). This  
521 activates the receptors serine/threonine kinase activity to phosphorylate and activate the  
522 receptor Smads 2/3 (Massagué *et al.*, 2005). In the model, receptors are simplified and  
523 represented as either bound or unbound complexes with their ligands. Phosphorylated  
524 Smads 2/3 (pSmad2/3) form heterodimers and translocate to the nucleus. pSmads com-  
525 plexes up-regulate other transcription factors, such as LEF-1. The pSmad2/4-LEF-1 com-  
526 plex has been shown to directly repress the E-cadherin gene (Nawshad *et al.*, 2007).  
527 LEF-1 also binds with  $\beta$ -catenin to upregulate mesenchymal proteins such as fibronectin  
528 (Medici *et al.*, 2011). In the model, Smad signaling is consolidated into a single Smad  
529 species that can act in a co-dependent fashion with LEF1 to downregulate E-cadherin via  
530 a transfer function, eliminating the need for an explicity LEF-1, pSmad complex. The EMT  
531 gene expression program was initiated by the binding of TGF- $\beta$  isoforms to TGF- $\beta$  sur-  
532 face receptors, starting the downstream signaling program. Repression of E-cadherin  
533 expression is the central event in the transition from an epithelial to a mesenchymal  
534 phenotype (Cano *et al.*, 2000). However, this transition is not solely driven by transcrip-  
535 tional events. At the protein level, the repression of E-cadherin leads to a release of  
536  $\beta$ -catenin from cell membrane. Cytosolic  $\beta$ -catenin then translocates to the nucleus and  
537 forms transcriptionally-active complexes with immunoglobulin transcription factor 2 (TCF-  
538 4) to drive TGF- $\beta$ 3 expression (Medici *et al.*, 2008). The PI3K to GSK3 pathway was  
539 included and acted as an activating mechanism of  $\beta$ -catenin signaling through TGF- $\beta$ 3  
540 signaling (Medici *et al.*, 2008). GSK3 is known to act on  $\beta$ -catenin signaling through APC  
541 complex associated ubiquitin-proteasome pathway. The APC complex is represented in  
542 our model and serves as a second reservoir of  $\beta$ -catein in untransformed cells whose  
543 sequestration is regulated by GSK3 (Larue & Bellacosa, 2005, Medici *et al.*, 2008, Zhou  
544 *et al.*, 2004). Lastly, VEGF-A activation of NFATc1 takes place through calcineurin sig-  
545 naling leading to an enhancement of E-cadherin expression (Suehiro *et al.*, 2014), as

546 supported by our VEGF-A experimental data (Fig. S4).

547 **Formulation, solution and analysis of the EMT model equations**

548 *EMT signaling events.* EMT signaling events were modeled using either saturation or

549 mass-action kinetics within an ordinary differential equation (ODE) framework:

$$\frac{1}{\tau_i} \frac{dx_i}{dt} = \sum_{j=1}^{\mathcal{R}} \sigma_{ij} r_j(\mathbf{x}, \epsilon, \mathbf{k}) - \mu x_i \quad i = 1, 2, \dots, \mathcal{M} \quad (1)$$

550 where  $\mathcal{R}$  denotes the number of signaling reactions and  $\mathcal{M}$  denotes the number of pro-  
551 teins in the model. The quantity  $\tau_i$  denotes a time scale parameter for species  $i$  which  
552 captures unmodeled effects. In the current study  $\tau_i = 1$  for all species. The quantity  
553  $r_j(\mathbf{x}, \epsilon, \mathbf{k})$  denotes the rate of reaction  $j$ . Typically, reaction  $j$  is a non-linear function of  
554 biochemical and enzyme species abundance, as well as unknown model parameters  $\mathbf{k}$   
555 ( $\mathcal{K} \times 1$ ). The quantity  $\sigma_{ij}$  denotes the stoichiometric coefficient for species  $i$  in reaction  $j$ . If  
556  $\sigma_{ij} > 0$ , species  $i$  is produced by reaction  $j$ . Conversely, if  $\sigma_{ij} < 0$ , species  $i$  is consumed  
557 by reaction  $j$ , while  $\sigma_{ij} = 0$  indicates species  $i$  is not connected with reaction  $j$ . Species  
558 balances were subject to the initial conditions  $\mathbf{x}(t_o) = \mathbf{x}_o$ .

559 Rate processes were written as the product of a kinetic term ( $\bar{r}_j$ ) and a control term ( $v_j$ )  
560 in the EMT model. The rate of enzyme catalyzed reactions was modeled using saturation  
561 kinetics:

$$\bar{r}_j = k_j^{cat} \epsilon_i \left( \frac{x_s}{K_{js} + x_s} \right) \quad (2)$$

562 where  $k_j^{cat}$  denotes the catalytic rate constant for reaction  $j$ ,  $\epsilon_i$  denotes the abundance of  
563 the enzyme catalyzing reaction  $j$ , and  $K_{js}$  denotes the saturation constant for species  $s$   
564 in reaction  $j$ . On the other hand, mass action kinetics were used to model protein-protein  
565 binding interactions within the network:

$$\bar{r}_j = k_j^{max} \prod_{s \in m_j^-} x_s^{-\sigma_{sj}} \quad (3)$$

566 where  $k_j^{max}$  denotes the maximum rate for reaction  $j$ ,  $\sigma_{sj}$  denotes the stoichiometric coefficient  
 567 for species  $s$  in reaction  $j$ , and  $s \in m_j$  denotes the set of *reactants* for reaction  $j$ .  
 568 We assumed all binding interactions were irreversible.

569 The control terms  $0 \leq v_j \leq 1$  depended upon the combination of factors which influenced  
 570 rate process  $j$ . For each rate, we used a rule-based approach to select from competing control factors.  
 571 If rate  $j$  was influenced by  $1, \dots, m$  factors, we modeled this relationship as  $v_j = \mathcal{I}_j(f_{1j}(\cdot), \dots, f_{mj}(\cdot))$  where  $0 \leq f_{ij}(\cdot) \leq 1$  denotes a regulatory transfer  
 572 function quantifying the influence of factor  $i$  on rate  $j$ . The function  $\mathcal{I}_j(\cdot)$  is an integration  
 573 rule which maps the output of regulatory transfer functions into a control variable. In this  
 574 study, we used  $\mathcal{I}_j \in \{\min, \max\}$  (Sagar & Varner, 2015). If a process has no modifying  
 575 factors,  $v_j = 1$ .

577 *EMT gene expression processes.* The EMT model described both signal transduction  
 578 and gene expression events following the addition of TGF- $\beta$  and VEGF-A. For each  
 579 gene, we modeled both the resulting mRNA ( $m_j$ ) and protein ( $p_j$ ):

$$\frac{dm_j}{dt} = r_{T,j} - (\mu + \delta_{m,j}) m_j + \lambda_j \quad (4)$$

$$\frac{dp_j}{dt} = r_{X,j} - (\mu + \delta_{p,j}) p_j \quad (5)$$

580 where  $j = 1, 2, \dots, \mathcal{G}$ . The terms  $r_{T,j}$  and  $r_{X,j}$  denote the specific rate of transcription,  
 581 and translation while the terms  $\delta_{m,j}$  and  $\delta_{p,j}$  denote degradation constants for mRNA and  
 582 protein, respectively. Lastly,  $\mu$  denotes the specific growth rate, and  $\lambda_j$  denotes the constitutive  
 583 rate of gene expression for gene  $j$ . The specific transcription rate was modeled  
 584 as the product of a kinetic term  $\bar{r}_{T,j}$  and a control term  $u_j$  which described how the abundance  
 585 of transcription factors, or other regulators influenced the expression of gene  $j$ .  
 586 The kinetic rate of transcription was modeled as:

$$\bar{r}_{T,j} = \alpha_j \left[ V_T^{max} \left( \frac{G_j}{K_T + G_j} \right) \right] \quad (6)$$

587 where the maximum gene expression rate was defined as the product of a character-  
 588 istic transcription rate constant ( $k_T$ ) and the abundance of RNA polymerase,  $V_T^{max} =$   
 589  $k_T (RNAP)$ . The parameter  $\alpha_j$  was used to adjust the transcription to that of gene  $j$  (es-  
 590 timated in this study), while  $k_T$ ,  $G_j$  and  $RNAP$  were estimated from literature (Milo *et al.*,  
 591 2010). Similar to the signaling processes, the gene expression control term  $0 \leq u_j \leq 1$   
 592 depended upon the combination of factors which influenced rate process  $j$ . For each  
 593 rate, we used a rule-based approach to select from competing control factors. If the ex-  
 594 pression of gene  $j$  was influenced by  $1, \dots, m$  factors, we modeled this relationship as  
 595  $u_j = \mathcal{I}_j(f_{1j}(\cdot), \dots, f_{mj}(\cdot))$  where  $0 \leq f_{ij}(\cdot) \leq 1$  denotes a regulatory transfer function  
 596 quantifying the influence of factor  $i$  on the expression of gene  $j$ . The function  $\mathcal{I}_j(\cdot)$  is an  
 597 integration rule which maps the output of regulatory transfer functions into a control vari-  
 598 able. In this study, we used  $\mathcal{I}_j \in \{\min, \max\}$  (Sagar & Varner, 2015). If a gene expression  
 599 process has no modifying factors,  $u_j = 1$ . Lastly, the specific translation rate was modeled  
 600 as:

$$r_{X,j} = \beta_j \left[ V_X^{max} \left( \frac{m_j}{K_X + m_j} \right) \right] \quad (7)$$

601 where  $V_X^{max}$  denotes a characteristic maximum translation rate estimated from literature,  
 602  $\beta_j$  denotes the transcript specific correction the characteristic translation rate, and  $K_X$   
 603 denotes a translation saturation constant. The characteristic maximum translation rate  
 604 was defined as the product of a characteristic translation rate constant ( $k_X$ ) and the abun-  
 605 dance of Ribosomes ( $RIBO$ ),  $V_X^{max} = k_X (RIBO)$ , where both  $k_X$  and  $RIBO$  abundance  
 606 were estimated from literature (Milo *et al.*, 2010). The values used for the characteristic  
 607 transcription and translation parameters are given in the supplemental materials.

608 The signaling and gene expression model equations were implemented in Julia and  
 609 solved using the CVODE routine of the Sundials package (Bezanson *et al.*, 2014, Hindmarsh  
 610 *et al.*, 2005). The model code and parameter ensemble is freely available under an MIT  
 611 software license and can be downloaded from <http://www.varnerlab.org>.

612 *Estimation of model parameters using multiobjective optimization.* The EMT model had  
613 296 unknown parameters (169 kinetic constants, 44 saturation constants, 38 control logic  
614 parameters, and 45 non-zero initial conditions) which were not uniquely identifiable given  
615 the training data. Instead, we estimated a population of likely models (each consistent  
616 with the training data) using 41 data sets generated in DLD1 colon carcinoma, MDCKII,  
617 and A375 melanoma cells taken from Medici *et al.* (Medici *et al.*, 2008). We used the  
618 Pareto Optimal Ensemble Technique (JuPOETs) multiobjective optimization framework in  
619 combination with leave-one-out cross-validation to estimate an ensemble of model param-  
620 eters (Bassen *et al.*, 2016, Song *et al.*, 2010). Cross-validation was used to calculate both  
621 training and prediction error during the parameter estimation procedure (Kohavi, 1995).  
622 The 41 intracellular protein and mRNA data-sets used for identification were organized  
623 into 11 objective functions. These 11 objective functions were then partitioned, where  
624 each partition contained ten training objectives and one validation objective. The training  
625 and validation data were Western blots. We achieved a physical simulation scale by estab-  
626 lishing characteristic rates of transcription, translation, mRNA and protein degradation, as  
627 well as characteristic concentrations of ribosomes and RNAPs (Milo *et al.*, 2010). The  
628 concentration scale is in nM, with proteins ranging from 10-1000nM and mRNA ranging  
629 from 0.01 to 1nM, reflecting the true abundances and ratios between each species.

630 **Cell culture and experimental interrogation** DLD1 colon carcinoma, MCF10A, and  
631 HUVEC were acquired from the American Tissue Culture Collection (Manassas, VA).  
632 Cells were grown in culture with RPMI 1640 medium with 10% fetal bovine serum and  
633 1% penicillin/streptomycin for DLD1, EBM-2 supplemented with EGM-2, 5% fetal bovine  
634 serum, and 1% penicillin/streptomycin for HUVEC, or MGEM 2 supplemented with insulin,  
635 bovine pituitary extract, cholera toxin, hEGF, hydrocortisone, 5% horse serum, and 1%  
636 penicillin/streptomycin for MCF10A. Cells were serum starved for 24 hours and removed  
637 from all experimental conditions. Recombinant VEGFA165 was also removed from cul-  
638 ture medium prior to experimentation. Recombinant human TGF- $\beta$ 2 (R & D Systems,

639 Minneapolis, MN) was added to the culture medium at a concentration of 10 ng/ml and re-  
640 combinant VEGFA165 at a concentration of (5ng/ml, 50ng/ml) for all relative experiments.  
641 NFAT inhibitor (VIVIT peptide) (EMDBiosciences, Darmstadt, Germany), was added to  
642 the culture medium at a concentration of 10 $\mu$ M for all relative experiments. Cells were  
643 passaged 1:3 or 1:4 every 3-6 d and used between passages 4 and 8.

644 *VEGF treatment* DLD1 and MCF10A cells were suspended in culture media (with RPMI  
645 1640 medium with 10% fetal bovine serum and 1% penicillin/streptomycin for DLD1 or  
646 MGEM 2 supplemented with insulin, bovine pituitary extract, cholera toxin, hEGF, hydro-  
647 cortisone, 5% horse serum, and 1% penicillin/streptomycin for MCF10A), and allowed to  
648 aggregate overnight in hanging drop culture (20 $\mu$ L; 20,000 cells). The spherical aggre-  
649 gates were placed on the surface of neutralized type I collagen hydrogels (1.5mg/mL)  
650 and allowed to adhere. Cultures were then serum starved (1% serum) for 24 hours. Re-  
651 combinant VEGFA165 was then added to the media (5ng/ml, 50ng/ml) and mRNA was  
652 harvested after 3hr and 24hr timepoint.

653 *RT-PCR* RNA extractions were performed using a Qiagen total RNA purification kit (Qi-  
654 agen, Valencia, CA) and RNA was reverse transcribed to cDNA using the SuperScript  
655 III RT-PCR kit with oligo(dT) primer (Invitrogen). Sufficient quality RNA was determined  
656 by an absorbance ratio A260/A280 of 1.8-2.1, while the quantity of RNA was determined  
657 by measuring the absorbance at 260nm (A260). Real-time PCR experiments were con-  
658 ducted using the SYBR Green PCR system (Biorad, Hercules, CA) on a Biorad CFX96  
659 cycler, with 40 cycles per sample. Cycling temperatures were as follows: denaturing,  
660 95C; annealing, 60C; and extension, 70C. Primers were designed to detect GAPDH, E-  
661 cadherin, vimentin, Slug, Sp1, and NFATc1 in cDNA clones: Sp1 (F-TTG AAA AAG GAG  
662 TTG GTG GC, R-TGC TGG TTC TGT AAG TTG GG, Accession NG030361.1), NFATc1  
663 (F-GCA TCA CAG GGA AGA CCG TGT C, R-GAA GTT CAA TGT CGG AGT TTC TGA  
664 G, Accession NG029226.1). GAPDH, E-cadherin, vimentin, and Slug primers were taken  
665 from previously published literature (Medici *et al.*, 2008).

666 *Antibody Staining* Samples were fixed in 4% PFA overnight at 4C. Samples were then  
667 washed for 15 minutes on a rocker 3 times with PBS, permeabilized with 0.2% Triton-X  
668 100 (VWR International, Radnor, PA) for 10 minutes, and washed another 3 times with  
669 PBS. Samples were incubated overnight at 4C in a 1% BSA (Rockland Immunochemi-  
670 cals, Inc., Gilbertsville, PA) blocking solution followed by another 4C overnight incubation  
671 with either rabbit anti-human E-cadherin 1:100 (Abcam, ab53033), mouse anti-human  
672 phospho-Sp1 1:100 (Abcam, ab37707), mouse anti-human vimentin 1:100 (Invitrogen,  
673 V9), and rabbit anti-human NFATc1 (Santa Cruz, sc-7294) 1:100. After 3 washes for 15  
674 minutes with PBS, samples were exposed to Alexa Fluor 488 or 568 conjugated (Invit-  
675 rogen), species specific secondary antibodies at 1:100 in 1% BSA for 2 hours at room  
676 temperature. Three more washes with PBS for 15 minutes were followed by incubation  
677 with either DRAQ5 far red nuclear stain (Enzo Life Sciences, Plymouth Meeting, PA) at  
678 1:1000.

679 *FACS* Flow cytometry for E-cadherin 1:100 (Abcam) and vimentin 1:100 expressing cells  
680 was performed. Briefly, cells were trypsinized, fixed with 4% PFA for 10 min and then pre-  
681 served in 50% methanol/PBS. Cells were kept in the -20C until antibody staining was  
682 preformed. Samples were divided into multiple aliquots in order to stain the proteins  
683 separately and compensate for secondary antibody non-specific binding. Cells were in-  
684 cubated for 24 hrs at 4 C in primary antibody diluted in either PBS (extracellular) or 0.2%  
685 saponin-PBS (intracellular). Cells were then washed 3 times with PBS and incubated  
686 with appropriate secondary antibodies and imaged using a Coulter Epics XL-MCL Flow  
687 Cytometer (Coulter). All samples were compensated using appropriate background sub-  
688 traction and all samples were normalized using 7500 cells per flow condition.

689 *Three-Dimensional Culture and Tubulogenesis Assays* For invasion/migration assays,  
690 cells were resuspended in culture media, and allowed to aggregate overnight in hanging  
691 drop culture (20 $\mu$ L; 20,000 cells). The spherical aggregates were placed on the surface of  
692 neutralized type I collagen hydrogels (1.5mg/mL) and allowed to adhere for 2 hrs before

adding treatments. Cultures were maintained for 72 hrs, after which they were fixed in 4% PFA and slowly rehydrated using PBS. For compaction assays, cells were pelleted via centrifugation and resuspended within a neutralized collagen hydrogel (1.5mg/mL) solution at a density of 400,000 cells/mL. 250 $\mu$ L of gel was inoculated into culture wells, which solidified after 60min. Treatments were then added within 800 $\mu$ L of the culture medium without serum. Gels were liberated from the surfaces of the culture wells the next day and cultured free floating for an additional 3-7 days, exchanging serum free media with appropriate factors every 48 hrs.

Tubulogenesis was defined as a typical nonmalignant acini structure. This includes a polarized epithelial cell, hollow lumen, and the basal sides of the cell are surrounded by ECM proteins (Fig. 6A, Controls or VEGF treated). Previous work has shown that change in the morphological characteristics of nontumorigenic MCF10A epithelial acini occur over time and exploiting them to growth in 3D culture can be quantified. For example, using image segmentation, Chang et al. (Chang *et al.*, 2007) examined the elongation of the MCF10A acini at 6, 12, and 96 hours after a particular treatment. Polizzotti et al. (Polizzotti *et al.*, 2012) also suggested a computational method to quantify acini structure based on morphological characteristics in nonmalignant, noninvasive, and invasive conditions. Adapted from these approaches, we first fluorescently labeled our cultures and captured the acini structures by 3D confocal microscopy. Next individual acini structures in the images were segmented by imageJ and labeled. We then extracted the number of ductal branches. Ductal branching was defined as any elongated cell cluster extending away from the total acini structure, which was manually segmented and counted using ImageJ. A total of 5 images for each condition were used, and approximately 12 acini were analyzed in each image. Total branching was normalized to the amount of acini present, and provides an overall general assessment to the extent of acini remodeling.

**Statistics** Results are expressed as mean  $\pm$  standard error,  $n \geq 6$ . Data was analyzed with the GraphPad Prism version 4.00 for Windows (GraphPad Software, San Diego,

<sup>720</sup> CA) and SAS (Statistical Analysis Software, Cary, NC). A one-way ANOVA with Tukey's  
<sup>721</sup> post hoc was used to compare differences between means and data was transformed  
<sup>722</sup> when necessary to obtain equal sample variances. Differences between means were  
<sup>723</sup> considered significant at  $p < 0.05$ .

724 **References**

- 725 Abramoff M, Magelhaes P, Ram S (2004) Image Processing with ImageJ. *Biophotonics International*, **11**: 36–42
- 726 Ahmed S, Nawshad A (2007) Complexity in interpretation of embryonic epithelial-mesenchymal transition in response to transforming growth factor-beta signaling. *Cells Tissues Organs* **185**: 131–45
- 727 Aramburu J, Yaffe MB, López-Rodríguez C, Cantley LC, Hogan PG, Rao A (1999) Affinity-driven peptide selection of an NFAT inhibitor more selective than cyclosporin A. *Science* **285**: 2129–33
- 728 730 Arce L, Pate KT, Waterman ML (2009) Groucho binds two conserved regions of LEF-1 for HDAC-dependent repression. *BMC Cancer* **9**: 159
- 731 733 Bailey JE (2001) Complex biology with no parameters. *Nat Biotechnol* **19**: 503–4
- 732 Bassen D, Vilkovoy M, Minot M, Butcher JT, Varner JD (2016) JuPOETs: A Constrained Multiobjective Optimization Approach to Estimate Biochemical Model Ensembles in the Julia Programming Language. *bioRxiv* **10.1101/056044**
- 733 739 Bezanson J, Edelman A, Karpinski S, Shah VB (2014) Julia: A Fresh Approach to Numerical Computing. *CoRR* **abs/1411.1607**
- 740 Bullock MD, Sayan AE, Packham GK, Mirnezami AH (2012) MicroRNAs: critical regulators of epithelial to mesenchymal (EMT) and mesenchymal to epithelial transition (MET) in cancer progression. *Biol Cell* **104**: 3–12
- 741 744 Butcher JT, Penrod AM, García AJ, Nerem RM (2004) Unique morphology and focal adhesion development of valvular endothelial cells in static and fluid flow environments. *Arterioscler Thromb Vasc Biol* **24**: 1429–34
- 742 747 Cano A, Pérez-Moreno MA, Rodrigo I, Locascio A, Blanco MJ, del Barrio MG, Portillo F, Nieto MA (2000) The transcription factor snail controls epithelial-mesenchymal transitions by repressing E-cadherin expression. *Nat Cell Biol* **2**: 76–83
- 748 750 Chang H, Park C, Parvin B (2007) Quantitative Representation of Three-dimensional Cell

- 751 Culture Models. In *Proceedings of the 2007 IEEE International Symposium on Biomed-*  
752 *ical Imaging: From Nano to Macro, Washington, DC, USA, April 12-16, 2007*. pp. 89–92
- 753 Chen WW, Schoeberl B, Jasper PJ, Niepel M, Nielsen UB, Lauffenburger DA, Sorger PK  
754 (2009) Input-output behavior of ErbB signaling pathways as revealed by a mass action  
755 model trained against dynamic data. *Mol Syst Biol* **5**: 239
- 756 Choi M, Shi J, Jung SH, Chen X, Cho KH (2012) Attractor landscape analysis reveals  
757 feedback loops in the p53 network that control the cellular response to DNA damage.  
758 *Sci Signal* **5**: ra83
- 759 Chung SW, Miles FL, Sikes RA, Cooper CR, Farach-Carson MC, Ogunnaike BA (2009)  
760 Quantitative modeling and analysis of the transforming growth factor beta signaling  
761 pathway. *Biophys J* **96**: 1733–50
- 762 Cirit M, Haugh JM (2012) Data-driven modelling of receptor tyrosine kinase signalling  
763 networks quantifies receptor-specific potencies of PI3K- and Ras-dependent ERK acti-  
764 vation. *Biochem J* **441**: 77–85
- 765 Creixell P, Schoof EM, Erler JT, Linding R (2012) Navigating cancer network attractors for  
766 tumor-specific therapy. *Nat Biotechnol* **30**: 842–8
- 767 Debnath J, Brugge JS (2005) Modelling glandular epithelial cancers in three-dimensional  
768 cultures. *Nat Rev Cancer* **5**: 675–88
- 769 Debnath J, Muthuswamy SK, Brugge JS (2003) Morphogenesis and oncogenesis of MCF-  
770 10A mammary epithelial acini grown in three-dimensional basement membrane cul-  
771 tures. *Methods* **30**: 256–268
- 772 Deryck R, Zhang YE (2003) Smad-dependent and Smad-independent pathways in TGF-  
773 beta family signalling. *Nature* **425**: 577–84
- 774 Dhasarathy A, Phadke D, Mav D, Shah RR, Wade PA (2011) The transcription factors  
775 Snail and Slug activate the transforming growth factor-beta signaling pathway in breast  
776 cancer. *PLoS One* **6**: e26514
- 777 Dhimolea E, Maffini MV, Soto AM, Sonnenschein C (2010) The role of collagen reorgani-

- 778 zation on mammary epithelial morphogenesis in a 3D culture model. *Biomaterials* **31**:  
779 3622–3630
- 780 Eastman Q, Grosschedl R (1999) Regulation of LEF-1/TCF transcription factors by Wnt  
781 and other signals. *Curr Opin Cell Biol* **11**: 233–40
- 782 Eisenberg LM, Markwald RR (1995) Molecular regulation of atrioventricular valvuloseptal  
783 morphogenesis. *Circ Res* **77**: 1–6
- 784 Ferrara N (2002) VEGF and the quest for tumour angiogenesis factors. *Nat Rev Cancer*  
785 **2**: 795–803
- 786 Gadkar KG, Varner J, Doyle FJ 3rd (2005) Model identification of signal transduction  
787 networks from data using a state regulator problem. *Syst Biol (Stevenage)* **2**: 17–30
- 788 Grumolato L, Liu G, Haremaiki T, Mungamuri SK, Mong P, Akiri G, Lopez-Bergami P, Arita  
789 A, Anouar Y, Mlodzik M, Ronai ZA, Brody J, Weinstein DC, Aaronson SA (2013) ?-  
790 Catenin-Independent Activation of TCF1/LEF1 in Human Hematopoietic Tumor Cells  
791 through Interaction with ATF2 Transcription Factors. *PLoS Genet* **9**: e1003603
- 792 Guaita S, Puig I, Franci C, Garrido M, Dominguez D, Batlle E, Sancho E, Dedhar S,  
793 De Herreros AG, Baulida J (2002) Snail induction of epithelial to mesenchymal transition  
794 in tumor cells is accompanied by MUC1 repression and ZEB1 expression. *J Biol Chem*  
795 **277**: 39209–16
- 796 Handl J, Kell DB, Knowles J (2007) Multiobjective optimization in bioinformatics and com-  
797 putational biology. *IEEE/ACM Trans Comput Biol Bioinform* **4**: 279–92
- 798 Hardy KM, Booth BW, Hendrix MJC, Salomon DS, Strizzi L (2010) ErbB/EGF signaling  
799 and EMT in mammary development and breast cancer. *J Mammary Gland Biol Neo-*  
800 *plasia* **15**: 191–9
- 801 Hasenauer J, Waldherr S, Doszczak M, Radde N, Scheurich P, Allgöwer F (2011) Iden-  
802 tification of models of heterogeneous cell populations from population snapshot data.  
803 *BMC Bioinformatics* **12**: 125
- 804 Hemavathy K, Ashraf SI, Ip YT (2000a) Snail/slug family of repressors: slowly going into

- 805 the fast lane of development and cancer. *Gene* **257**: 1–12
- 806 Hemavathy K, Guru SC, Harris J, Chen JD, Ip YT (2000b) Human Slug is a repressor that  
807 localizes to sites of active transcription. *Mol Cell Biol* **20**: 5087–95
- 808 Hindmarsh A, Brown P, Grant K, Lee S, Serban R, Shumaker D, Woodward C (2005) SUN-  
809 DIALS: Suite of nonlinear and differential/algebraic equation solvers. *ACM Transactions*  
810 *on Mathematical Software* **31**: 363–396
- 811 Hong JP, Li XM, Li MX, Zheng FL (2013) VEGF suppresses epithelial-mesenchymal tran-  
812 sition by inhibiting the expression of Smad3 and miR-192 a Smad3-dependent mi-  
813 croRNA. *Int J Mol Med* **31**: 1436–42
- 814 Huber MA, Azoitei N, Baumann B, Grünert S, Sommer A, Pehamberger H, Kraut N, Beug  
815 H, Wirth T (2004) NF-kappaB is essential for epithelial-mesenchymal transition and  
816 metastasis in a model of breast cancer progression. *J Clin Invest* **114**: 569–81
- 817 Hyduke DR, Palsson BØ (2010) Towards genome-scale signalling network reconstruc-  
818 tions. *Nat Rev Genet* **11**: 297–307
- 819 Jackstadt R, Röh S, Neumann J, Jung P, Hoffmann R, Horst D, Berens C, Bornkamm  
820 GW, Kirchner T, Menssen A, Hermeking H (2013) AP4 is a mediator of epithelial-  
821 mesenchymal transition and metastasis in colorectal cancer. *J Exp Med* **210**: 1331–50
- 822 Jensen LJ, Kuhn M, Stark M, Chaffron S, Creevey C, Muller J, Doerks T, Julien P, Roth  
823 A, Simonovic M, Bork P, von Mering C (2009) STRING 8—a global view on proteins and  
824 their functional interactions in 630 organisms. *Nucleic Acids Res* **37**: D412–6
- 825 Jiang YG, Luo Y, He DI, Li X, Zhang LI, Peng T, Li MC, Lin YH (2007) Role of Wnt/beta-  
826 catenin signaling pathway in epithelial-mesenchymal transition of human prostate can-  
827 cer induced by hypoxia-inducible factor-1alpha. *Int J Urol* **14**: 1034–9
- 828 Kalita MK, Sargsyan K, Tian B, Paulucci-Holthauzen A, Najm HN, Debusschere BJ,  
829 Brasier AR (2011) Sources of cell-to-cell variability in canonical nuclear factor-kB (NF-  
830 kB) signaling pathway inferred from single cell dynamic images. *J Biol Chem* **286**:  
831 37741–57

- 832 Kim K, Lu Z, Hay ED (2002) Direct evidence for a role of beta-catenin/LEF-1 signaling  
833 pathway in induction of EMT. *Cell Biol Int* **26**: 463–76
- 834 Kohavi R (1995) A study of cross-validation and bootstrap for accuracy estimation and  
835 model selection. In *International joint Conference on artificial intelligence*, vol. 14. Cite-  
836 seer, pp. 1137–1145
- 837 Larue L, Bellacosa A (2005) Epithelial-mesenchymal transition in development and can-  
838 cer: role of phosphatidylinositol 3' kinase/AKT pathways. *Oncogene* **24**: 7443–54
- 839 Lee MW, Vassiliadis VS, Park JM (2009) Individual-based and stochastic modeling of cell  
840 population dynamics considering substrate dependency. *Biotechnol Bioeng* **103**: 891–9
- 841 Lequieu J, Chakrabarti A, Nayak S, Varner JD (2011) Computational modeling and anal-  
842 ysis of insulin induced eukaryotic translation initiation. *PLoS Comput Biol* **7**: e1002263
- 843 Lian Yg, Zhou Qg, Zhang Yj, Zheng Fl (2011) VEGF ameliorates tubulointerstitial fibrosis  
844 in unilateral ureteral obstruction mice via inhibition of epithelial-mesenchymal transition.  
845 *Acta Pharmacol Sin* **32**: 1513–21
- 846 Linding R, Jensen LJ, Osthimer GJ, van Vugt MATM, Jørgensen C, Miron IM, Diella F,  
847 Colwill K, Taylor L, Elder K, Metalnikov P, Nguyen V, Pascalescu A, Jin J, Park JG, Sam-  
848 son LD, Woodgett JR, Russell RB, Bork P, Yaffe MB, et al. (2007) Systematic discovery  
849 of in vivo phosphorylation networks. *Cell* **129**: 1415–26
- 850 Luan D, Szlam F, Tanaka KA, Barie PS, Varner JD (2010) Ensembles of uncertain mathe-  
851 matical models can identify network response to therapeutic interventions. *Mol Biosyst*  
852 **6**: 2272–86
- 853 Machta BB, Chachra R, Transtrum MK, Sethna JP (2013) Parameter space compression  
854 underlies emergent theories and predictive models. *Science* **342**: 604–7
- 855 Mancini M, Toker A (2009) NFAT proteins: emerging roles in cancer progression. *Nat Rev*  
856 *Cancer* **9**: 810–820
- 857 Massagué J, Seoane J, Wotton D (2005) Smad transcription factors. *Genes Dev* **19**:  
858 2783–810

- 859 Medici D, Hay ED, Goodenough DA (2006) Cooperation between snail and LEF-1 trans-  
860 scription factors is essential for TGF-beta1-induced epithelial-mesenchymal transition.  
861 *Mol Biol Cell* **17**: 1871–9
- 862 Medici D, Hay ED, Olsen BR (2008) Snail and Slug promote epithelial-mesenchymal tran-  
863 sition through beta-catenin-T-cell factor-4-dependent expression of transforming growth  
864 factor-beta3. *Mol Biol Cell* **19**: 4875–87
- 865 Medici D, Potenta S, Kalluri R (2011) Transforming growth factor-?2 promotes  
866 Snail-mediated endothelial-mesenchymal transition through convergence of Smad-  
867 dependent and Smad-independent signalling. *Biochem J* **437**: 515–520
- 868 Milo R, Jorgensen P, Moran U, Weber G, Springer M (2010) BioNumbers—the database  
869 of key numbers in molecular and cell biology. *Nucleic Acids Res* **38**: D750–3
- 870 Moles CG, Mendes P, Banga JR (2003) Parameter estimation in biochemical pathways: a  
871 comparison of global optimization methods. *Genome Res* **13**: 2467–74
- 872 Morris MK, Saez-Rodriguez J, Clarke DC, Sorger PK, Lauffenburger DA (2011) Training  
873 signaling pathway maps to biochemical data with constrained fuzzy logic: quantitative  
874 analysis of liver cell responses to inflammatory stimuli. *PLoS Comput Biol* **7**: e1001099
- 875 Nagy JA, Dvorak AM, Dvorak HF (2007) VEGF-A and the induction of pathological angio-  
876 genesis. *Annu Rev Pathol* **2**: 251–75
- 877 Nawshad A, Hay ED (2003) TGFbeta3 signaling activates transcription of the LEF1 gene  
878 to induce epithelial mesenchymal transformation during mouse palate development. *J  
879 Cell Biol* **163**: 1291–301
- 880 Nawshad A, Medici D, Liu CC, Hay ED (2007) TGFbeta3 inhibits E-cadherin gene expres-  
881 sion in palate medial-edge epithelial cells through a Smad2-Smad4-LEF1 transcription  
882 complex. *J Cell Sci* **120**: 1646–53
- 883 Neve RM, Chin K, Fridlyand J, Yeh J, Baehner FL, Fevr T, Clark L, Bayani N, Coppe JP,  
884 Tong F, Speed T, Spellman PT, DeVries S, Lapuk A, Wang NJ, Kuo WL, Stilwell JL,  
885 Pinkel D, Albertson DG, Waldman FM, *et al.* (2006) A collection of breast cancer cell

- 886 lines for the study of functionally distinct cancer subtypes. *Cancer Cell* **10**: 515–27
- 887 Niessen K, Fu Y, Chang L, Hoodless PA, McFadden D, Karsan A (2008) Slug is a direct  
888 Notch target required for initiation of cardiac cushion cellularization. *J Cell Biol* **182**:  
889 315–25
- 890 O'Brien LE, Tang K, Kats ES, Schutz-Geschwender A, Lipschutz JH, Mostov KE (2004)  
891 ERK and MMPs sequentially regulate distinct stages of epithelial tubule development.  
892 *Dev Cell* **7**: 21–32
- 893 Park SY, Lee HE, Li H, Shipitsin M, Gelman R, Polyak K (2010) Heterogeneity for stem  
894 cell-related markers according to tumor subtype and histologic stage in breast cancer.  
895 *Clin Cancer Res* **16**: 876–87
- 896 Pearson GW, Hunter T (2007) Real-time imaging reveals that noninvasive mammary ep-  
897 ithelial acini can contain motile cells. *J Cell Biol* **179**: 1555–67
- 898 Polizzotti L, Basak O, Bjornsson C, Shubert K, Yener B, Plopper G (2012) Novel Image  
899 Analysis Approach Quantifies Morphological Characteristics of 3D Breast Culture Acini  
900 with Varying Metastatic Potentials. *J Biomed Biotech* **2012**: 1–16
- 901 Polyak K, Weinberg RA (2009) Transitions between epithelial and mesenchymal states:  
902 acquisition of malignant and stem cell traits. *Nat Rev Cancer* **9**: 265–273
- 903 Rodriguez-Fernandez M, Rehberg M, Kremling A, Banga JR (2013) Simultaneous model  
904 discrimination and parameter estimation in dynamic models of cellular systems. *BMC  
905 Syst Biol* **7**: 76
- 906 Sagar A, Varner JD (2015) Dynamic Modeling of the Human Coagulation Cascade Using  
907 Reduced Order Effective Kinetic Models. *Processes* **3**: 178
- 908 Sainani KL (2012) Meet the Skeptics: Why some doubt biomedical models - and what it  
909 takes to win them over. *Biomedical Computation Review* : 12 – 18
- 910 Schoeberl B, Eichler-Jonsson C, Gilles ED, Muller G (2002) Computational modeling of  
911 the dynamics of the MAP kinase cascade activated by surface and internalized EGF  
912 receptors. *Nat Biotechnol* **20**: 370–375

- 913 Singh G, Singh SK, König A, Reutlinger K, Nye MD, Adhikary T, Eilers M, Gress TM,  
914 Fernandez-Zapico ME, Ellenrieder V (2010) Sequential activation of NFAT and c-Myc  
915 transcription factors mediates the TGF-beta switch from a suppressor to a promoter of  
916 cancer cell proliferation. *J Biol Chem* **285**: 27241–50
- 917 Song SO, Chakrabarti A, Varner JD (2010) Ensembles of signal transduction models  
918 using Pareto Optimal Ensemble Techniques (POETs). *Biotechnol J* **5**: 768–80
- 919 Stahl PJ, Felsen D (2001) Transforming growth factor-beta, basement membrane, and  
920 epithelial-mesenchymal transdifferentiation: implications for fibrosis in kidney disease.  
921 *Am J Pathol* **159**: 1187–92
- 922 Strauss R, Li ZY, Liu Y, Beyer I, Persson J, Sova P, Möller T, Pesonen S, Hemminki A,  
923 Hamerlik P, Drescher C, Urban N, Bartek J, Lieber A (2011) Analysis of epithelial and  
924 mesenchymal markers in ovarian cancer reveals phenotypic heterogeneity and plastic-  
925 ity. *PLoS One* **6**: e16186
- 926 Suehiro Ji, Kanki Y, Makihara C, Schadler K, Miura M, Manabe Y, Aburatani H, Kodama  
927 T, Minami T (2014) Genome-wide approaches reveal functional vascular endothelial  
928 growth factor (VEGF)-inducible nuclear factor of activated T cells (NFAT) c1 binding to  
929 angiogenesis-related genes in the endothelium. *J Biol Chem* **289**: 29044–59
- 930 Sullivan NJ, Sasser AK, Axel AE, Vesuna F, Raman V, Ramirez N, Oberyszyn TM, Hall BM  
931 (2009) Interleukin-6 induces an epithelial-mesenchymal transition phenotype in human  
932 breast cancer cells. *Oncogene* **28**: 2940–7
- 933 Swain PS, Elowitz MB, Siggia ED (2002) Intrinsic and extrinsic contributions to stochas-  
934 ticity in gene expression. *Proc Natl Acad Sci U S A* **99**: 12795–800
- 935 Tasseff R, Nayak S, Song SO, Yen A, Varner JD (2011) Modeling and analysis of retinoic  
936 acid induced differentiation of uncommitted precursor cells. *Integr Biol (Camb)* **3**: 578–  
937 591
- 938 Terfve C, Cokelaer T, Henriques D, MacNamara A, Goncalves E, Morris MK, van Iersel M,  
939 Lauffenburger DA, Saez-Rodriguez J (2012) CellINOptR: a flexible toolkit to train protein

- 940 signaling networks to data using multiple logic formalisms. *BMC Syst Biol* **6**: 133
- 941 Thiery JP (2003) Epithelial-mesenchymal transitions in development and pathologies.
- 942 *Curr Opin Cell Biol* **15**: 740–6
- 943 Vega S, Morales AV, Ocaña OH, Valdés F, Fabregat I, Nieto MA (2004) Snail blocks the
- 944 cell cycle and confers resistance to cell death. *Genes Dev* **18**: 1131–43
- 945 Vilar JMG, Jansen R, Sander C (2006) Signal processing in the TGF-beta superfamily
- 946 ligand-receptor network. *PLoS Comput Biol* **2**: e3
- 947 Villaverde AF, Banga JR (2014) Reverse engineering and identification in systems biology:
- 948 strategies, perspectives and challenges. *J R Soc Interface* **11**: 20130505
- 949 Wayman J, Varner J (2013) Biological systems modeling of metabolic and signaling net-
- 950 works. *Curr Opin Chem Eng* **2**: 365 – 372
- 951 Welch-Reardon KM, Wu N, Hughes CCW (2014) A Role for Partial Endothelial-
- 952 Mesenchymal Transitions in Angiogenesis? *Arterioscler Thromb Vasc Biol*
- 953 Willis BC, Borok Z (2007) TGF-beta-induced EMT: mechanisms and implications for fi-
- 954 brotic lung disease. *Am J Physiol Lung Cell Mol Physiol* **293**: L525–34
- 955 Wu Y, Deng J, Rychahou PG, Qiu S, Evers BM, Zhou BP (2009) Stabilization of snail by
- 956 NF-kappaB is required for inflammation-induced cell migration and invasion. *Cancer*
- 957 *Cell* **15**: 416–28
- 958 Xu J, Lamouille S, Derynck R (2009) TGF-beta-induced epithelial to mesenchymal transi-
- 959 tion. *Cell Res* **19**: 156–72
- 960 Zajchowski DA, Bartholdi MF, Gong Y, Webster L, Liu HL, Munishkin A, Beauheim C,
- 961 Harvey S, Ethier SP, Johnson PH (2001) Identification of gene expression profiles that
- 962 predict the aggressive behavior of breast cancer cells. *Cancer Res* **61**: 5168–78
- 963 Zavadil J, Böttlinger EP (2005) TGF-beta and epithelial-to-mesenchymal transitions.
- 964 *Oncogene* **24**: 5764–74
- 965 Zhou BP, Deng J, Xia W, Xu J, Li YM, Gunduz M, Hung MC (2004) Dual regulation of Snail
- 966 by GSK-3beta-mediated phosphorylation in control of epithelial-mesenchymal transi-

967 tion. *Nat Cell Biol* **6**: 931–40

## Extracellular

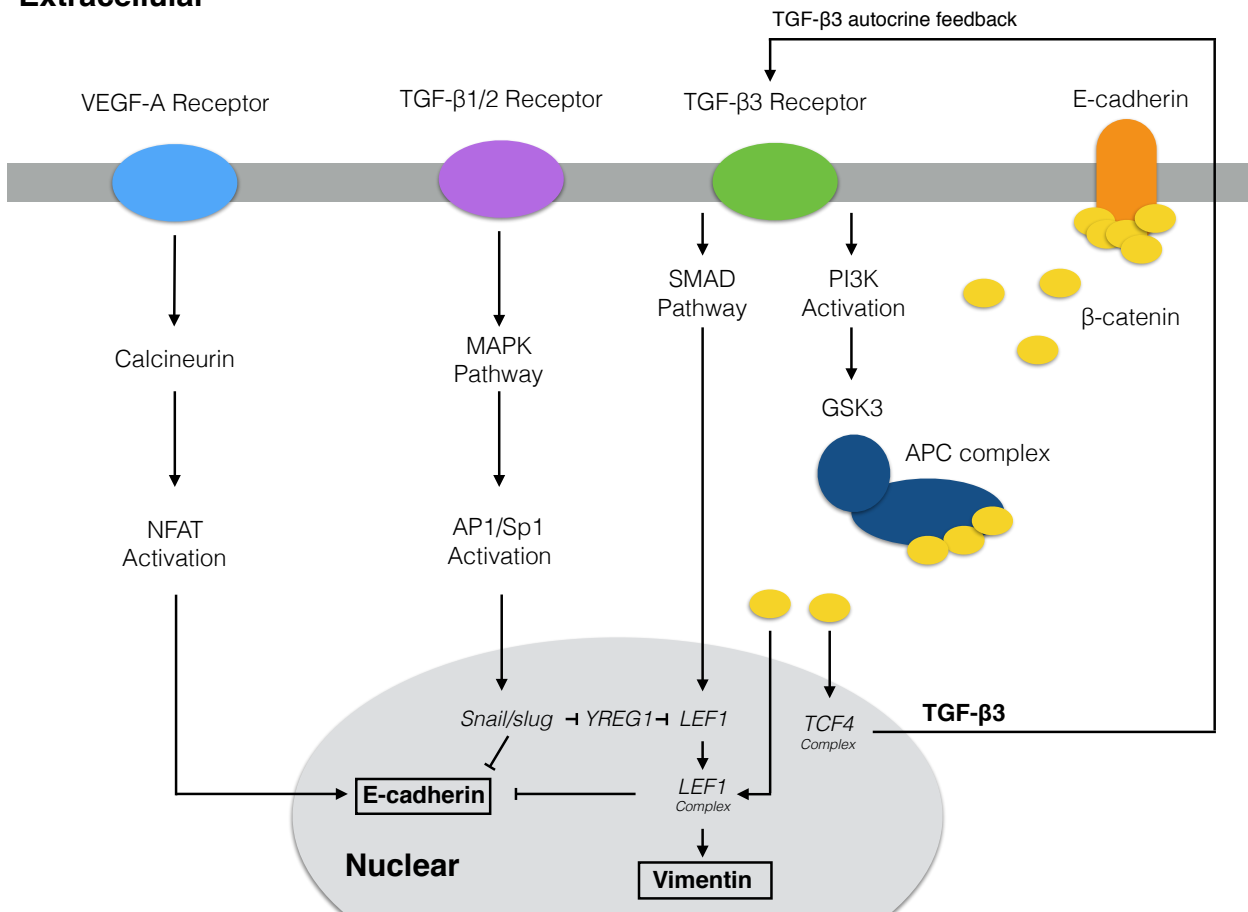


**Fig. 1:** Model connectivity recreates the core architecture during EMT. The EMT network contains 97 nodes (proteins, mRNA, and genes) interconnected by 169 interactions. Central to EMT induction, activation of the MAPK cascade occurs through TGF- $\beta$ 1/2 binding which activates the AP-1/Sp1 transcriptional axis. AP-1/Sp1 drives an autocrine response of TGF- $\beta$ 3, which activates the Smad cascade, leading to phenotypic change. Conversely, VEGF-A binding can stabilize an epithelial phenotype through NFAT activation. Downstream activation of  $\beta$ -catenin signaling due to E-cadherin loss and GSK3 inactivation of  $\beta$ -cateinin confinement is critical to the complete activation of the EMT program. The complete list of molecular interactions that comprise the model is given in the supplement.

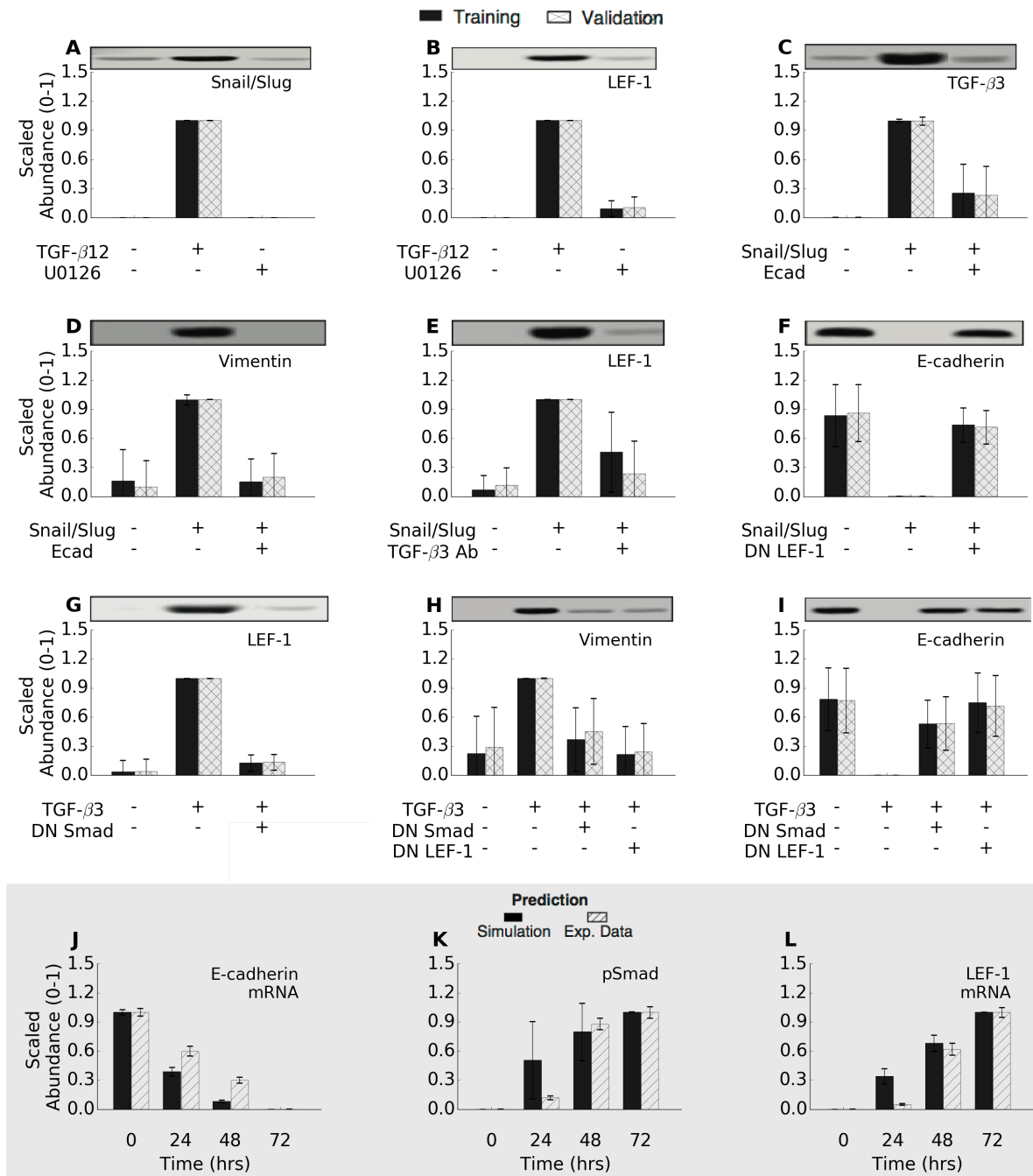


**Fig. 2:** Training and validation simulations. The population of EMT models qualitatively captured TGF- $\beta$ -induced EMT signaling. (A-I) The population was generated using JuPOETs and trained using 11 different objective functions (41 data sets) taken from Medici *et al.* (Medici *et al.*, 2008). The model captured the simulated experiments for all cases when compared to randomized controls. (J-L) The model populations were also compared against untrained temporal data to measure the effectiveness as a pure prediction.

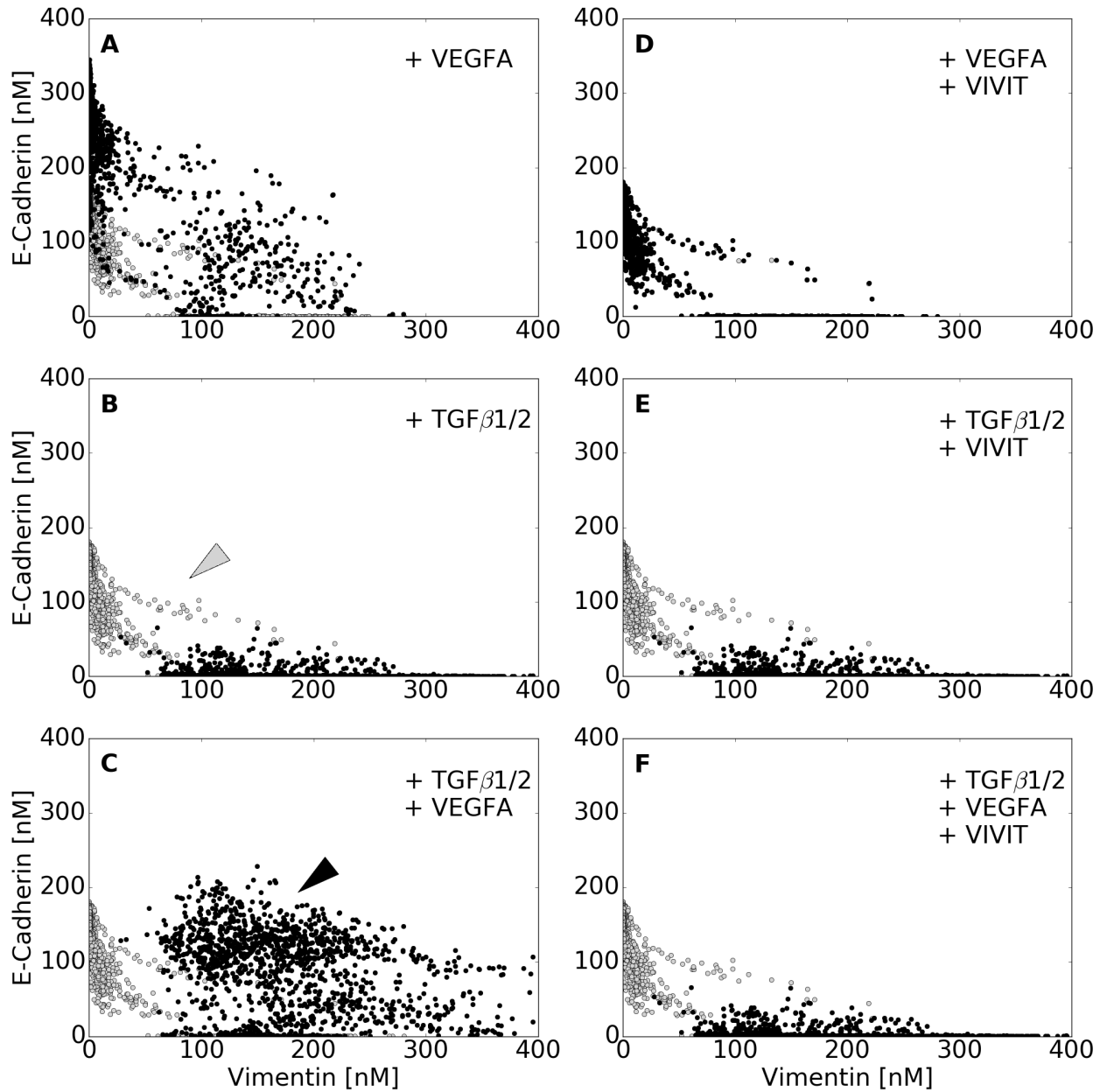


**Fig. 3:** Simulated VEGF-A and TGF- $\beta$ 1/2 exposure promoted phenotype heterogeneity. Simulated response to TGF- $\beta$ 1/2 and VEGF-A exposure with and without axis specific inhibitors. Vimentin and E-cadherin abundances (in nM) were used to quantify the shift in population at 48 hrs. (A-C) VEGF-A (50 a.u.) treatment resulted in a population with enhanced epithelial properties. This was contrary to the addition of TGF- $\beta$ 2 (10 a.u.), which shifted the population towards a mesenchymal phenotype. Interestingly, the combined effects of TGF- $\beta$ 2 and VEGFA was found to increase both ecadherin and vimentin levels, creating a heterogeneous population (black arrow), which can also be seen in a minority of untreated cells (gray arrow). (D-F) To isolate the effect of NFAT, we inhibited NFAT de-phosphorylation in combination with VEGFA. This negated the increase in ecadherin expression and shifted the population towards a mesenchymal phenotype. Likewise, combining NFAT inhibition with TGF- $\beta$  mitigated all VEGF enhanced ecadherin expression. Lastly, combination of TGF- $\beta$ 2, VEGFA, and NFAT inhibition nearly mitigated all effects of VEGFA, shifting the heterogeneous population towards a mesenchymal phenotype. In whole, high levels of phosphorylated-Sp1 correlated with vimentin expression, while NFAT was responsible for maintaining E-cadherin expression in the presence of other factors, although neither were mutually exclusive.

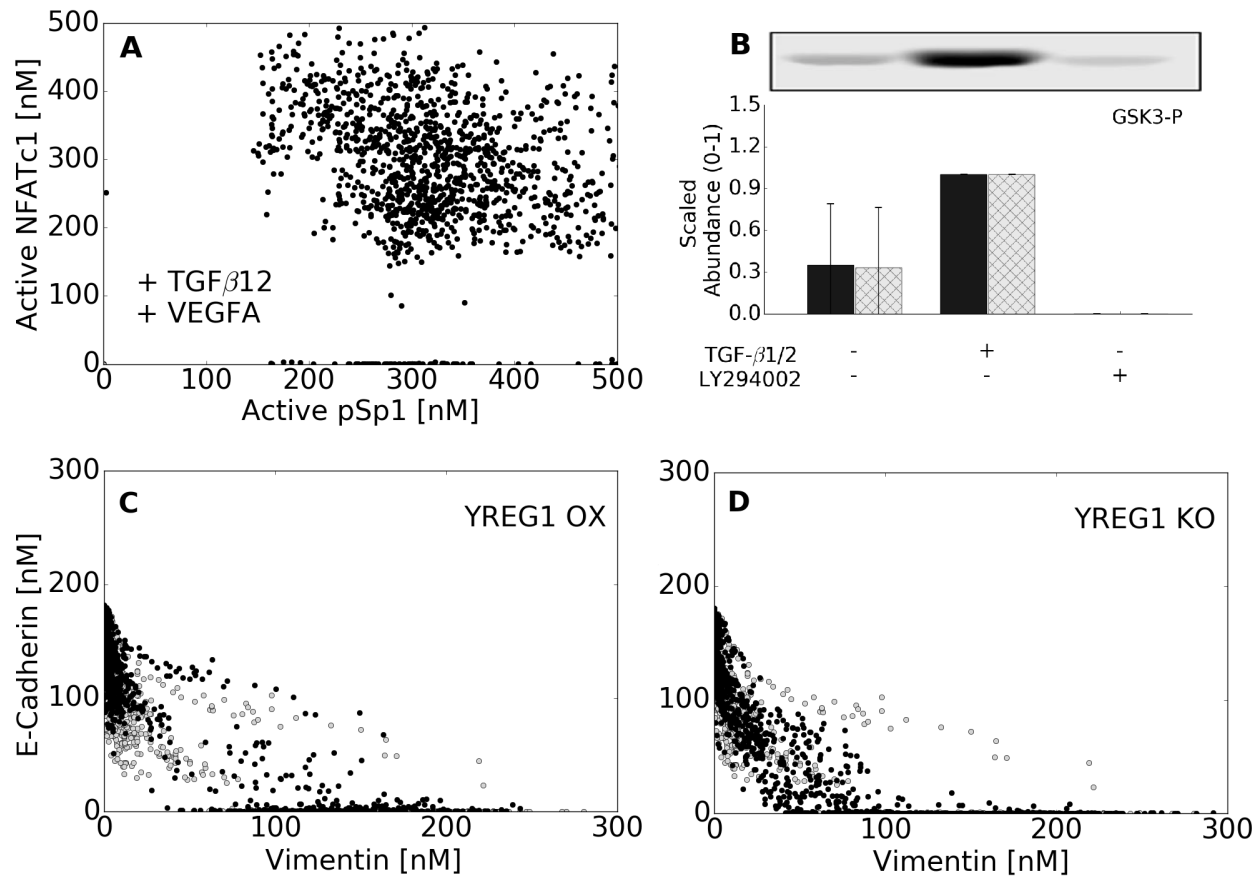


**Fig. 4:** Analysis of underlying signaling responses. (A) We examined the distribution of NFATc1 and AP1/SP1 in cells containing the hybrid phenotype (VEGF-A + TGF- $\beta$ 2 case), showing the potential for cells to express both SP1 and NFATc1 in a non exclusive manner. (B) We were able to show a fit to an additional objective demonstrating the activation of GSK3 through PI3K. Our model captures this activation through TGF- $\beta$ 3 signaling. LY294002 is a PI3K inhibitor. (C) We identified a novel regulator of LEF1 called YREG1 that allows Snail/Slug to emulate an inducer by repressing YREG1, which was required to stabilize the untreated population. YREG1 overexpression revealed an enhanced epithelial phenotype, while some inherently transformed cells moved towards a hybrid phenotype. (D) In the absence of YREG1, most of the population failed to consistently retain a stable epithelial state.

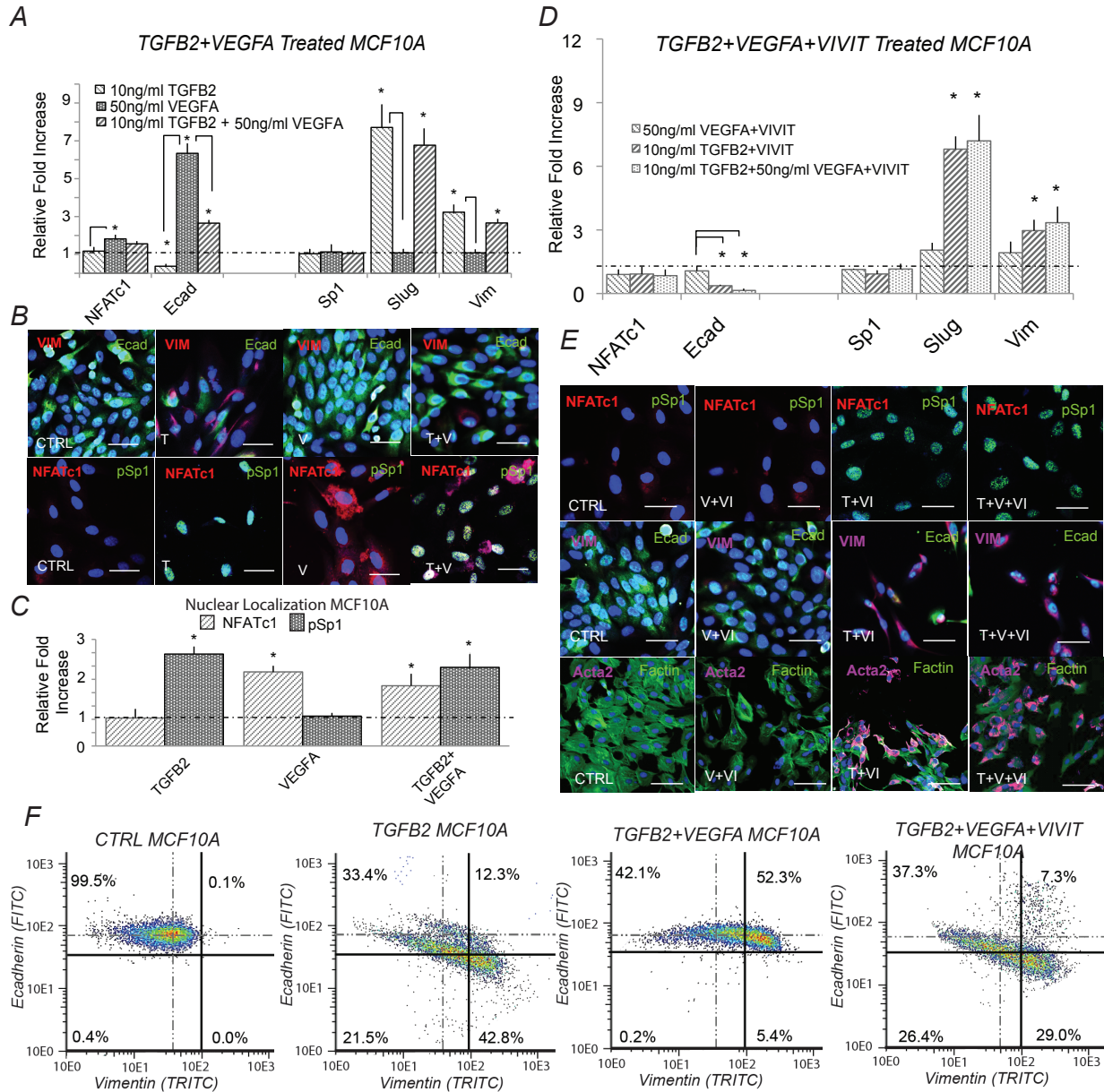


**Fig. 5:** Simultaneous TGF- $\beta$ 1/2 and VEGF-A treatment induced phenotype heterogeneity and is dependent upon NFAT activity *in-vitro*. (A) In MCF10A, treatment with (10ng/ml) TGF- $\beta$ 2 increased Slug and vimentin, while ecadherin expression was inhibited at both the gene and protein level at 48 hrs. Conversely, VEGFA alone increased both NFATc1 and ecadherin gene expression. Simultaneous TGF- $\beta$ 2 (10ng/ml) and VEGFA (50ng/ml) treatment increased Slug, NFATc1, and vimentin expression, while also increasing ecadherin levels via qPCR. (B-C) Immunofluorescence confirmed these results and nuclear co-localization of both phospho-Sp1 and NFAT were found dependent upon TGF- $\beta$ 2 and VEGFA, respectively. (D) To isolate the effect of NFAT, treatment of VEGFA (50ng/ml) and VIVIT (10 $\mu$ M) reduced ecadherin expression at 48hrs (control-dashed line). Similarly, combined TGF- $\beta$ 2, VEGFA and VIVIT treatment increased Slug and vimentin expression, while inhibiting ecadherin levels via qPCR. (E) These findings were confirmed via immunofluorescence as the VIVIT peptide inhibited ecadherin and nuclear localization of NFATc1 in all three cases. (F) Quantitative flow cytometry also confirmed this trend. Similar experiments in DLD1 followed a similar trend (supplement). Magnification, 40x. Scale bars: 50 $\mu$ m. C=Control, T=TGF- $\beta$ 2 , V=VEGFA, VI= NFAT inhibitor (VIVIT). Asterisks signify statistical differences from each other according to a one-way ANOVA with Tukey's post hoc ( $p < 0.05$ ).

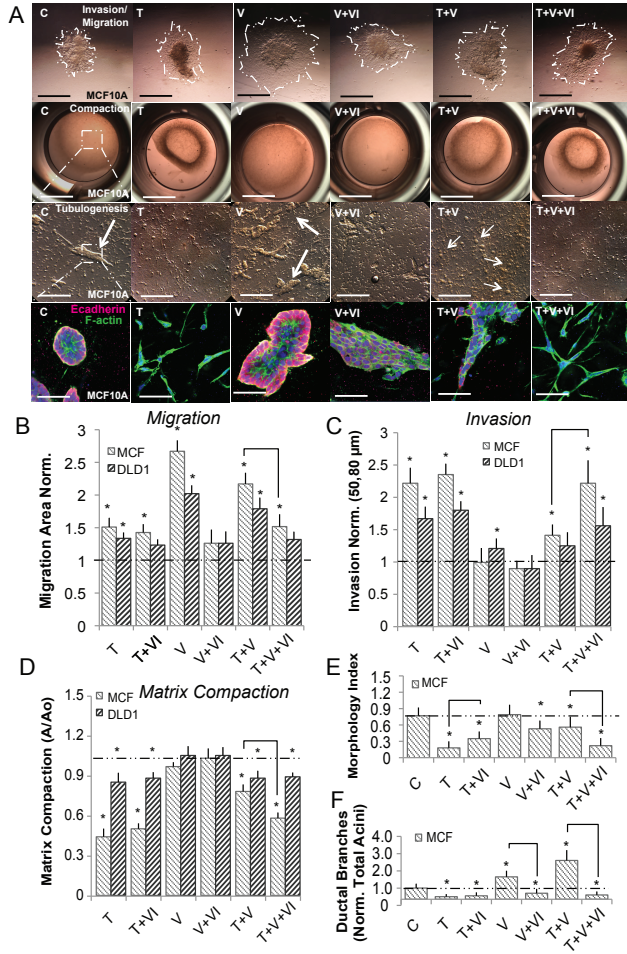


**Fig. 6:** Ductal branching is dependent upon phenotype heterogeneity within MCF10A in 3-D culture. MCF10A and DLD1 were formed into spheroids overnight and explanted to a collagen gel for 72 hrs. For compaction and tubular assays, cells were embedded into collagen gels for 72 hrs, and the extent of tubulogenesis was measured at 7 days. (A-D) Within MCF10A, TGF- $\beta$ 2 (10ng/ml) enhanced invasion and contractile properties while, VEGFA (50ng/ml) promoted increased migration. TGF- $\beta$ 2 with VEGFA significantly increased migration, while limiting with compaction. VIVIT (10 $\mu$ M) in combination with VEGFA and TGF- $\beta$ 2 decreased migration and compaction, while increasing invasion. (D) Likewise, cell morphology (circularity index) correlated with both invasion and compaction in MCF10A. (E-F) The size of tubular structures (acini) also increased significantly upon addition of VEGFA, while the number of ductal branches was most significant upon simultaneous TGF- $\beta$ 2 and VEGFA treatment (Red-Ecadherin, Green-Factin, Blue-Nuclear). DLD1 cells followed a similar trend, although the degree of migration, invasion, and compaction was less significant. In addition, no tubular structures were identified during the 7 day tubulogenesis endpoints. Scale bars: 500 $\mu$ m, 1000 $\mu$ m, 250 $\mu$ m, and 80 $\mu$ m, respectively. C=Control, T=TGF- $\beta$ 2 , V=VEGFA, VI= NFAT inhibitor (VIVIT). Asterisks signify statistical differences from each other according to a one-way ANOVA with Tukey's post hoc ( $p < 0.05$ ). Boxes in the left-most panel identify regions identified by arrows that were then imaged in greater zoom in the panel immediately below. The box diagram was not repeated for arrows in the other panels for clarity, but the same method was applied.

## Supplemental Materials and Methods

**Characteristic transcription and translation parameters.** We used literature based transcription and translation parameters to establish the characteristic synthesis and degradation rates for both mRNA and protein. We estimated values for the rate parameters from the Bionumbers database (Milo *et al.*, 2010). These parameters were then used for all gene expression calculations:

```
-----  
# Description  
-----  
  
cell_diameter = 12 # \mu m  
number_of_rnapII = 75000 # copies/cells  
number_of_ribosome = 1e6 # copies/cells  
mRNA_half_life_TF = 2 # hrs  
protein_half_life = 10 # hrs  
doubling_time = 19.5 # hrs  
max_translation_rate = 5 # aa/sec  
max_transcription_rate = 6.0 # nt/sec  
average_transcript_length = 15000 # nt  
average_protein_length = 5000 # aa  
fraction_nucleus = 0.49 # dimensionless  
av_number = 6.02e23 # number/mol  
avg_gene_number = 2 # number of copies of a gene  
-----  
  
-----  
# Description  
-----  
  
# Calculate the volume (units: L)  
V = ((1-fraction_nucleus)*(1/6)*(3.14159)*(hl60_diameter)^3)*(1e-15)  
  
# Calculate the rnapII_concentration and ribosome_concentration (units: nM)  
rnapII_concentration = number_of_rnapII*(1/av_number)*(1/V)*1e9  
ribosome_concentration = number_of_ribosome*(1/av_number)*(1/V)*1e9  
  
# degradation rate constants (units: hr^-1)  
degradation_constant_mRNA = -(1/mRNA_half_life_TF)*log(0.5)  
degradation_constant_protein = -(1/protein_half_life)*log(0.5)  
  
# kcats for transcription and translation (units: hr^-1)  
kcat_transcription = max_transcription_rate*(3600/average_transcript_length)  
kcat_translation = max_translation_rate*(3600/average_protein_length)  
  
# Maximum specific growth rate (units: hr^-1)  
maximum_specific_growth_rate = (1/doubling_time)*log(2)  
  
# What is the average gene concentration (units: nM)  
avg_gene_concentration = avg_gene_number*(1/av_number)*(1/V)*1e9  
  
# Cell death constant (units: hr^-1)  
death_rate_constant = 0.2*maximum_specific_growth_rate
```

```

# Saturation constants for translation and transcription (units: nM)
saturation_transcription = 4600*(1/av_number)*(1/V)*1e9
saturation_translation = 100000*(1/av_number)*(1/V)*1e9
-----
```

**Estimation and cross-validation of EMT model parameters.** We used the Pareto Optimal Ensemble Technique (POETs) multiobjective optimization framework in combination with leave-one-out cross-validation to estimate an ensemble of TGF- $\beta$ /EMT models. Cross-validation was used to calculate both training and prediction error during the parameter estimation procedure (Kohavi, 1995). The 41 intracellular protein and mRNA data-sets used for identification were organized into 11 objective functions. These 11 objective functions were then partitioned, where each partition contained ten training objectives and one validation objective. POETs integrates standard search strategies e.g., Simulated Annealing (SA) or Pattern Search (PS) with a Pareto-rank fitness assignment (Bassen *et al.*, 2016, Song *et al.*, 2010). Denote a candidate parameter set at iteration  $i + 1$  as  $\mathbf{k}_{i+1}$ . The squared error for  $\mathbf{k}_{i+1}$  for training set  $j$  was defined as:

$$E_j(\mathbf{k}) = \sum_{i=1}^{\mathcal{T}_j} \left( \hat{\mathcal{M}}_{ij} - \hat{y}_{ij}(\mathbf{k}) \right)^2 \quad (\text{S1})$$

The symbol  $\hat{\mathcal{M}}_{ij}$  denotes scaled experimental observations (from training set  $j$ ) while  $\hat{y}_{ij}$  denotes the scaled simulation output (from training set  $j$ ). The quantity  $i$  denotes the sampled time-index and  $\mathcal{T}_j$  denotes the number of time points for experiment  $j$ . In this study, the experimental data used for model training was typically the band intensity from Western or Northern blots. Band intensity was estimated using the ImageJ software package (Abramoff *et al.*, 2004). The scaled measurement for species  $x$  at time  $i = \{t_1, t_2, \dots, t_n\}$  in condition  $j$  is given by:

$$\hat{\mathcal{M}}_{ij} = \frac{\mathcal{M}_{ij} - \min_i \mathcal{M}_{ij}}{\max_i \mathcal{M}_{ij} - \min_i \mathcal{M}_{ij}} \quad (\text{S2})$$

O#	Species (protein)	Cell Type	Training	Prediction	Random
O1	LEF1	DLD1 CC,MDCKII,A375 MC	0.54 ± 0.167	0.505 ± 0.175	1.765 ± 0.223
O2	Vimentin	DLD1 CC,MDCKII,A375 MC	1.044 ± 0.668	0.783 ± 0.666	2.098 ± 0.784
O3	TGF $\beta$ 3	DLD1 CC,MDCKII,A375 MC	0.119 ± 0.262	0.225 ± 0.418	1.408 ± 0.732
O4	E-cadherin	DLD1 CC,MDCKII,A375 MC	2.299 ± 0.449	2.154 ± 0.625	3.459 ± 0.643
O5	$\beta$ -catenin	DLD1 CC,MDCKII,A375 MC	0.752 ± 0.38	0.514 ± 0.351	1.025 ± 0.0
O6	TGF $\beta$ 3	DLD1 CC,MDCKII,A375 MC	1.662 ± 0.55	1.54 ± 0.677	3.328 ± 0.981
O7	GSK3-P	DLD1 CC,MDCKII,A375 MC	0.19 ± 0.291	0.203 ± 0.292	0.756 ± 0.309
O8	LEF1	DLD1 CC,MDCKII,A375 MC	0.023 ± 0.078	0.03 ± 0.11	0.937 ± 0.298
O9	E-Cadherin	DLD1 CC,MDCKII,A375 MC	1.092 ± 1.228	1.412 ± 1.348	2.652 ± 1.435
O10	Snail/Slug	DLD1 CC,MDCKII,A375 MC	0.019 ± 0.0	0.019 ± 0.0	1.111 ± 0.744
O11	LEF1	DLD1 CC,MDCKII,A375 MC	0.005 ± 0.015	0.013 ± 0.06	0.797 ± 0.431

**Fig. S1:** Training and prediction values as a function of condition for the 11 TGF- $\beta$  objective functions versus a random parameter control.

Under this scaling, the lowest intensity band equaled zero while the highest intensity band equaled one. A similar scaling was defined for the simulation output. By doing this scaling, we trained the model on the relative change in blot intensity, over conditions or time (depending upon the experiment). Thus, when using multiple data sets (possibly from different sources) that were qualitatively similar but quantitatively different e.g., slightly different blot intensities over time or condition, we captured the underlying trends in the scaled data. JuPOETs is free or charge, open source and available for download under an MIT software license from <http://www.varnerlab.org>. Details of the JuPOETs implementation, including example codes are presented in Bassen *et al.*, (Bassen *et al.*, 2016).

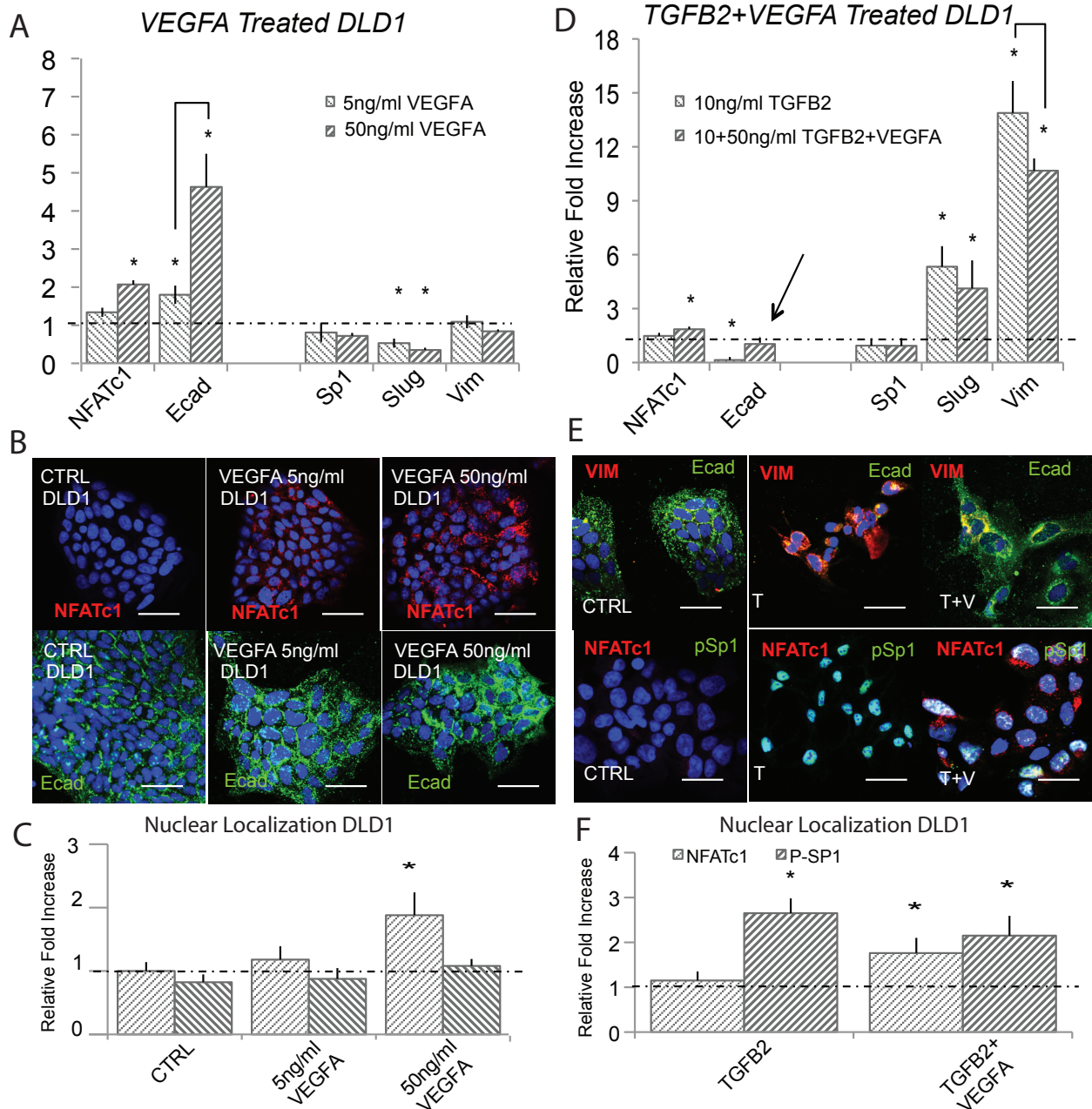


**Fig. S2:** VEGF-A attenuates TGF- $\beta$ 1/2 to induce phenotype heterogeneity in DLD1. (A) In DLD1, we found that 5ng/ml of VEGFA increased NFATc1 and E-cadherin gene expression via qPCR and 50ng/ml potentiated this effect at 48 hrs. (B - C) These findings were confirmed at the protein level via immunofluorescence, as ecadherin levels and nuclear localization of NFATc1 increased. (D) Treatment with (10ng/ml) TGF $\beta$ 2 resulted in mesenchymal transformation as measured via qPCR against target genes Slug, ecadherin, vimentin, Sp1, and NFATc1. (E - F) Immunofluorescence and nuclear localization revealed a strong presence of phospho-Sp1. (G) Combination of VEGFA (50ng/ml) and TGF $\beta$ 2 (10ng/ml) treatment resulted in increased Slug, NFATc1, and vimentin expression, while also increasing ecadherin levels compared to control. (H) Immunofluorescence confirmed these results, as both ecadherin and vimentin levels were elevated. (I) A significant increase in nuclear localization of both NFATc1 and phospho-Sp1 were also found. Magnification, 40x. Scale bars: 50 $\mu$ m. C=Control, T=TGF $\beta$ 2 , V=VEGFA, VI=NFAT inhibitor (VIVIT). Asterisks signify statistical differences from each other according to a one-way ANOVA with Tukey's post hoc ( $p < 0.05$ ).

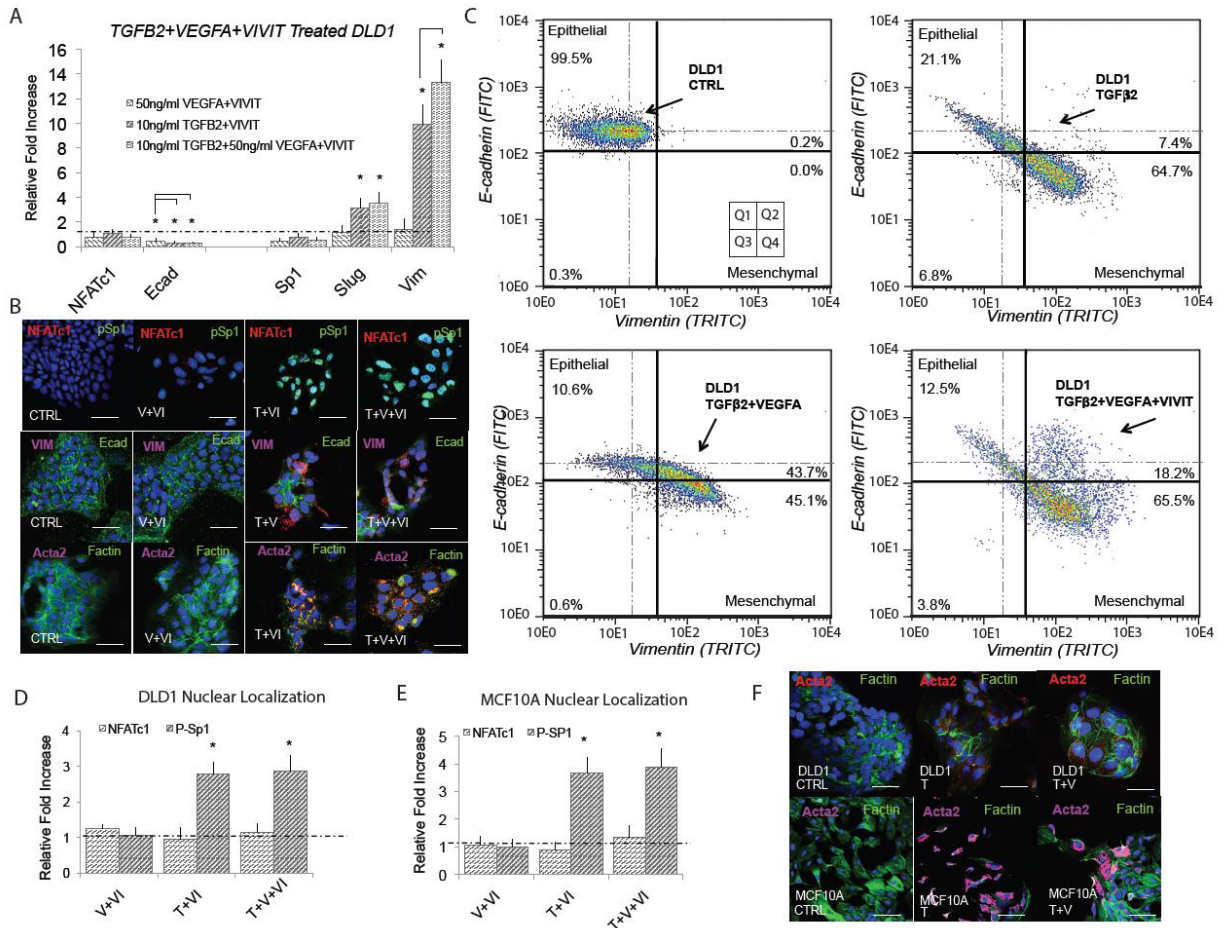


**Fig. S3:** E-cadherin expression is dependent upon NFAT activity in DLD1. (A) Treatment with VEGFA (50ng/ml) and NFAT inhibitory peptide VIVIT (10 $\mu$ M) resulted in significantly reduced ecadherin expression (qRT-PCR at 48hrs). Addition of TGF $\beta$ 2 (10ng/ml) and VIVIT resulted in increased Slug and vimentin expression, while inhibiting ecadherin levels. Combined TGF $\beta$ 2, VEGFA, and VIVIT treatment resulted in target genes Slug and vimentin expression increased, while inhibiting ecadherin levels. No change in Sp1 or NFATc1 expression was found. (B) These findings were confirmed via immunofluorescence as the VIVIT inhibitors was shown to inhibit ecadherin levels in all three cases. We also found no change in gene or nuclear localization of NFATc1 in all three cases, while phospho-Sp1 was found to increase in both TGF $\beta$  conditions. (C) Quantitative flow cytometry also confirmed this trend. (D,E) TGF $\beta$ 2, VEGFA and VIVIT treatment in DLD1 and MCF10A resulted in no change of Sp1 expression or NFATc1 expression. (F) Likewise, no change in nuclear localization of NFAT in all three cases, however phospho-Sp1 was found to increase in both TGF $\beta$  conditions. Magnification, 40x. Scale bars: 50 $\mu$ m. C=Control, T=TGF $\beta$ 2, V=VEGFA, VI= NFAT inhibitor (VIVIT). Asterisks signify statistical differences from each other according to a one-way ANOVA with Tukey's post hoc ( $p < 0.05$ ).

PRELIMINARY DATA USED TO HANDFIT RESPONSE OF VEGFA WITHIN SYSTEM

		MCF10A						
VEGFA		Relative mRNA			Normalized			
		Ecad	Slug	Vim	Ecad	Slug	Vim	
	5ng/ml	3HR	1.31	1.04	0.93	0.00	1.00	1.00
		48 HR	3.60	1.03	0.91	0.45	0.94	0.88
50ng/ml		3HR	1.37	0.92	0.88	0.01	0.25	0.71
		48 HR	6.34	0.88	0.76	1.00	0.00	0.00
Standard Deviation								
VEGFA		Relative mRNA			Normalized			
		Ecad	Slug	Vim	Ecad	Slug	Vim	
		5ng/ml	0.89	0.03	0.02	0.00	0.03	0.02
50ng/ml		3HR	0.78	0.03	0.27	0.10	0.03	0.26
		48 HR	0.11	0.10	0.53	0.00	0.03	0.43
VEGFA		Relative mRNA			Normalized			
		Ecad	Slug	Vim	Ecad	Slug	Vim	
5ng/ml		3HR	1.21	0.76	1.03	0.00	1.00	0.76
		48 HR	1.80	0.53	1.09	0.17	0.44	1.00
50ng/ml		3HR	1.54	0.46	1.03	0.10	0.27	0.76
		48 HR	4.63	0.35	0.84	1.00	0.00	0.00
Standard Deviation								
VEGFA		Relative mRNA			Normalized			
		Ecad	Slug	Vim	Ecad	Slug	Vim	
		5ng/ml	0.80	0.10	0.18	0.00	0.13	0.13
50ng/ml		3HR	0.24	0.12	0.17	0.02	0.10	0.16
		48 HR	0.89	0.19	0.45	0.06	0.11	0.33
VEGFA		Absolute mRNA			Normalized			
		Ecad	Slug	Vim	Ecad	Slug	Vim	
5ng/ml		3HR	0.94	88.12	10.23	0.00	1.00	1.00
		48 HR	2.10	55.64	5.45	0.40	0.41	0.40
50ng/ml		3HR	1.44	64.10	8.43	0.17	0.56	0.77
		48 HR	3.85	33.40	2.32	1.00	0.00	0.00
Standard Deviation								
VEGFA		Absolute mRNA			Normalized			
		Ecad	Slug	Vim	Ecad	Slug	Vim	
		5ng/ml	0.21	22.34	2.45	0.00	0.25	0.24
50ng/ml		3HR	0.45	15.55	1.12	0.09	0.11	0.08
		48 HR	0.38	17.87	2.23	0.05	0.16	0.20
VEGFA		3HR	1.30	9.46	0.45	0.34	0.00	0.00

**Fig. S4:** VEGF-A qPCR data used to hand fit VEGF enhancement of E-cadherin expression. mRNA was harvested after 3hr and 24hr timepoint.